Interaction of 2D Excitonic Complexes with their Environment

By

Andrey R. Klots

Dissertation

Submitted to the Faculty of the

Graduate School of Vanderbilt University

in partial fulfillment of the requirements

for the degree of

DOCTOR OF PHILOSOPHY

in

Physics

December 16, 2017

Nashville, Tennessee

Approved:

Kirill I. Bolotin, Ph.D

Sokrates Pantelides, Ph.D

Richard Haglund, Ph.D

Jason Valentine, Ph.D

Momchil Velkovsky, Ph.D

ACKNOWLEDGMENTS

I want to thank my friends and co-workers who helped me to work on my research. I appreciate many years of work and friendship with Dr. Dhiraj Prasai, Dr. AKM Newaz, Dr. Ryan Nicholl and many other friends at Vanderbilt, including, but not limited to Benjamin Weintrub, Austin Howes, Jason Bonacum, Dr. Borislav Ivanov, Dr. Bin Wang, Dr. Wenyi Wang, Andrey Baydin, Dr. Halina Krzyzanowska. All of these people contributed greatly to my research progress, helped me to learn and grow professionally and, of course, supported with good and interesting conversations. I also thank John Fellenstein for teaching me a about machining and fabricating most complicated parts. Particular notice should be given to Dr. Kirill A. Velizhanin for teaching useful approaches to condensed matter theory. Our group also acknowledges ONR N000141310299 for support. I want to especially thank my advisor Kirill Bolotin for great help in questions of science and professional development.

ABSTRACT

Two-dimensional materials are one of the most intensively studied systems in the modern solid state physics. Among the broad variety of currently known 2D materials, monolayer transition metal dichalcogenides (TMDC) are especially interesting. These materials exhibit strong light-matter interactions due to the presence of various types of excitons – bound states of charged carriers. Since every atom of a 2D material belongs to the surface, excitons in TMDCs are strongly influenced by their environment. Therefore, in order to understand the physical properties of 2D excitons it is critical to understand how these excitons interact with their environment. In this work, we study one of the most prominent interaction mechanisms – electromagnetic coupling between 2D excitons and their environment. We start with investigating basic properties of excitons in pristine suspended TMDCs decoupled from the environment. We reveal the exciton types, determine their binding energies and uncover dissociation mechanisms. Then, we probe relatively simple interaction mechanism – resonant energy transfer between 2D excitons and their environment. We demonstrate that rate of such interactions can be controlled by changing the Fermi level of the 2D material. Finally, we investigate a more complex phenomenon – dynamic, or frequency-dependent, screening of excitons by environment. We develop a simple theoretical model to understand dynamic screening and then experimentally test our predictions.

TABLE OF CONTENTS

Page

LIST OF FIGURES

Figure Page

LIST OF PUBLICATIONS

Klots AR, Weintrub B, Prasai D, Kidd D, Varga K, Velizhanin KA, et al. "Controlled dynamic screening of excitonic complexes in 2D semiconductors". arXiv preprint arXiv:170304707 (2017)

Prasai D, Klots AR, Newaz AKM, Niezgoda JS, Orfield NJ, Escobar CA, et al. "Electrical Control of near-Field Energy Transfer between Quantum Dots and Two-Dimensional Semiconductors". Nano Letters (2015)

Wang W, Klots A, Prasai D, Yang Y, Bolotin KI, Valentine J. "Hot electron-based near-infrared photodetection using bilayer MoS_2". Nano Letters (2015)

Wang W, Klots A, Yang Y, Li W, Kravchenko II, Briggs DP, et al. "Enhanced absorption in two-dimensional materials via Fano-resonant photonic crystals". Applied Physics Letters (2015)

Klots AR, Newaz AKM, Wang B, Prasai D, Krzyzanowska H, Lin J, et al. "Probing excitonic states in suspended two-dimensional semiconductors by photocurrent spectroscopy". Scientific Reports (2014)

CHAPTER 1. INTRODUCTION AND FIELD OVERVIEW

1.1. Introduction

Motivation

Two-dimensional (2D) materials is a topic of great interest in the solid state physics research community. Multiple reasons are responsible for such popularity: (i) Two-dimensional materials, like other low-dimensional systems have high surface-to volume ratio which makes them easily controllable via their environment[1-4]. (ii) Many of 2D materials are readily available in nature. Fabrication of devices and samples based on 2D materials is relatively simple and cheap in comparison with other low-dimensional systems like 2D electron gases (2DEGs) and topological insulators[5,6]. (iii) Most importantly, rich physics of low-dimensional systems allows one to observe properties and phenomena that are rarely found in other materials: strong interactions between charged carriers, high carrier mobility, half-integer quantum Hall effect, and other unusual electrical and optical effects[2,6-10]. In this thesis, we will focus on control of electric interactions between charged particles in 2D materials. We will study how environment influences properties of 2D quasiparticles: charge carriers and their bound states known as excitons. For example, interparticle interactions may be affected by screening due to the medium surrounding the 2D material, or by energy or charge transfer from the 2D material to the environment. Since these processes strongly depend on specific properties of 2D material's environment such as dielectric function, absorption coefficient, etc., it is very important to understand the physics of various environmental effects. Such understanding would allow us to account for environmental effects when obtaining any new data or interpreting already existing experimental results. Using optical and electrooptical techniques we study how environment affects electrooptical properties of 2D quasiparticles. On the one hand, this influence can often be

detrimental: e.g. scattering, uncontrollable doping. On the other hand, we also investigate how environment helps to manipulate various degrees of freedom in 2D materials and consider practical applications of our research results.

Excitonic complexes in 2D materials.

Current research involves many types of 2D materials such as semimetallic graphene and insulating hexagonal boron nitride (hBN). However, our main focus is on 2D semiconductors, mainly the family of monolayer (1L) transition metal dichalcogenides. Typical members of the TMDC family are MoS_2, WS_2, $MoSe_2$, and WSe_2. Existence of tightly-bound hydrogen-like

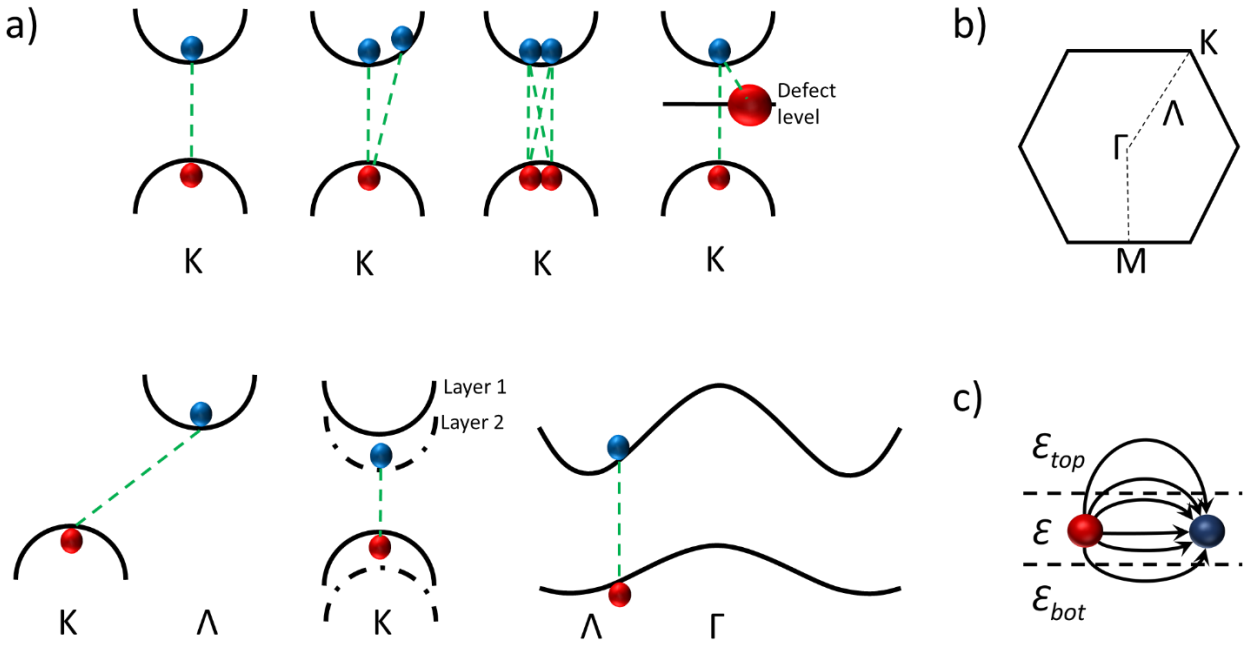

Figure 1.1. Types of excitonic complexes/excitonic species. (a) Band-structure diagrams. From left to right: neutral exciton, charged exciton (trion), biexciton, defect-bound exciton with positively-charged defect, indirect exciton, interlayer exciton, Mexican-hat C-exciton. Blue and red spheres represent negative and positive charges respectively. Green dashed lines represent attractive interactions. **(b)** Schematics of the TMDC Brillouin zone. **(c)** Schematic representations of electric field lines, created by charged particles and screened by the environment.

quasiparticles – excitons – is one of the most interesting features of TMDCs. Due to high effective mass of ~0.5m_0[11,12], low dimensionality and reduced screening, 2D excitons possess large binding energies of 300~700meV[2,10] and, having quantum yield of ~0.1%[13], are optically active and observable even at room temperature. Currently, a plethora of excitons and excitonic complexes (Fig.1.1) has been discovered in TMDCs[2,7-10,14]: **neutral exciton** consisting of one electron (e) and one hole (h); **trion** also known as charged exciton (2e+h or 2h+e) – neutral exciton bound to the charge carrier already present in the material; **defect-bound exciton** (e+h+defect); **indirect exciton** where e and h exist in different valleys – typically **K**- and **Λ**-valleys as well as more exotic excitons, such as **C-exciton** – a neutral exciton associated with the van-Hove singularity or band nesting around the **Γ**-point of the Brillouin zone; **interlayer exciton** existing in two- or more-layer structures, where e and h exist in separate layers; **biexciton** (2e+2h), etc...

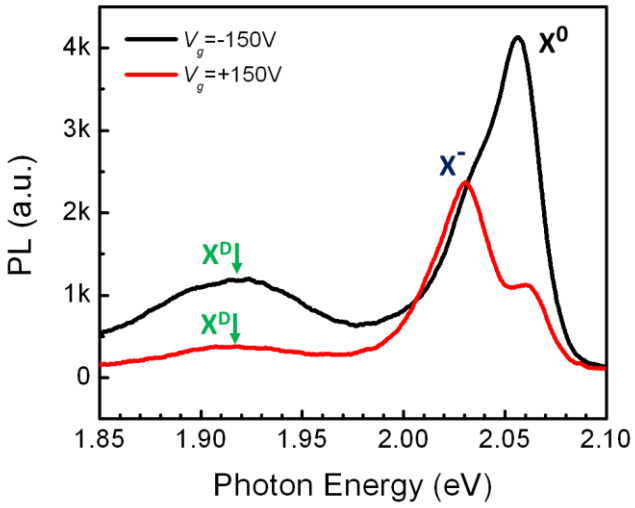

Figure 1.2. Photoluminescence spectra of TMDC (WS_2) excitons obtained at low (black curve) and high (red curve) doping levels. In the spectra three peaks are distinguishable. They stem from the neutral exciton (X^0), trion (X^-) and defect-bound exciton (X^D). Note that change of the doping level, achieved via electrostatic gating, described below strongly affects heights of the excitonic peaks.

Moreover, these excitonic states are coupled with spin-orbit-splitting of TMDC valence and sometimes conduction bands and can be selectively excited with polarized light. The most commonly used technique for observing these excitons experimentally is photoluminescence (PL) spectroscopy. For example, PL peaks, stemming from some of the excitonic complexes, namely, neutral, charged and defect-bound exciton are shown in Fig.1.2. The two curves in Fig.1.2 where obtained from the same sample, but at different doping levels. Note that magnitude and even positions of excitonic peaks depend on the Fermi level which can be controlled via electrostatic doping of the sample. Below, in section 1.3 we will discuss the mechanisms of such doping-dependence.

Screening of electric fields in 2D materials

The most obvious example of environmental effects on 2D materials is electrostatic screening of interparticle interactions. Due to low-dimensionality, electric field lines binding the e-h pair are largely located outside of the 2D material[2] and hence can be strongly screened by the environment. Because of the screening of electric fields, effective electric potential in a 2D material is no longer described by the Coulomb equation. Instead, charged particles in TMDCs interact via the so-called Keldysh potential[15], which is a solution of the Poisson equation for a thin dielectric layer stacked between two other dielectric materials with different dielectric constants:

$$V(\rho)=\frac{\pi}{\varepsilon d}\left[H_0\left(\frac{2\varepsilon'}{\varepsilon d}\rho\right)-Y_0\left(\frac{2\varepsilon'}{\varepsilon d}\rho\right)\right]. \qquad (1.1.1)$$

Here ρ is the distance between the interacting charges located in a 2D material, d is the thickness of a 2D material, which is typically Angstroms, ε is 2D material's dielectric constant,

$\varepsilon' = (\varepsilon_{bot} + \varepsilon_{top})/2$ is the average dielectric constant of surrounding top and bottom materials, and H_0, Y_0 are the Struve function and the Bessel function of the second kind respectively. It is interesting to consider a limit-case behavior of (1.1.1): at large distances of $\rho >> \varepsilon d/\varepsilon'$, Keldysh potential reduces to a simple Coulomb potential $V \approx 1/\varepsilon'\rho$, while at small distances of $\rho << \varepsilon d/\varepsilon'$ the potential becomes logarithmic: $V \approx (2/\varepsilon d)\ln(\varepsilon d/\varepsilon'\rho)$. Typically, TMDCs are deposited on a SiO_2 substrate with $\varepsilon_{bot} \sim 3$ and are surrounded by vacuum on top, while the dielectric constant of TMDC itself is $\varepsilon \sim 15$. Characteristic exciton size in TMDCs is 1~2nm[16] while TMDC thickness is about 0.7nm. Thus, the second limit case of $\rho \sim 1nm << \varepsilon d/\varepsilon' \sim 5nm$ is more relevant. This means that the electric potential in TMDCs decays logarithmically with distance. Interestingly, such distance-dependence of electric potential also takes place the solution of the two-dimensional Poisson equation. Thus, TMDC excitons can be considered truly two-dimensional: not only charged particles are confined in two dimensions, but even electric potential takes a two-dimensional form. This non-Coulombic interaction potential leads to the unusual non-hydrogenic Rydberg series in 2D excitons[2,16].

In order to visualize the effects of screening it is instructive to compare PL of defect-bound excitons in different environments: air and water (Fig.1.3). When water is deposited on top of a 2D material, electric field of a charged defect is screened out by water molecules. This leads to notable decrease of the exciton binding energy, manifested as a ~40meV blue-shift of the PL peak. This shows that environment indeed has a strong effect on 2D excitons.

Before proceeding to investigation of exciton-medium interactions we will first briefly discuss main properties of most common 2D materials. Then we will discuss most relevant mechanisms through which 2D materials interact with the environment. Although we have just

discussed one of these interactions – screening, in section 1.3 we will put screening in a much broader context of various other types of 2D material-medium interactions. In the end of this chapter, the outline of the current work will be formulated. In the next chapter we will report our study of pristine suspended TMDC samples, not interacting with any environment. In chapters 3 and 4, we will proceed to investigating electromagnetic interactions between TMDCs and their environment: from energy exchange to frequency-dependent dynamic screening.

1.2. Low-dimensional materials involved in the current work

Currently existing family of 2D materials already includes around a hundred members ranging from insulators to superconductors. In our research we involve only few of them. Below we will discuss prominent properties of these materials:

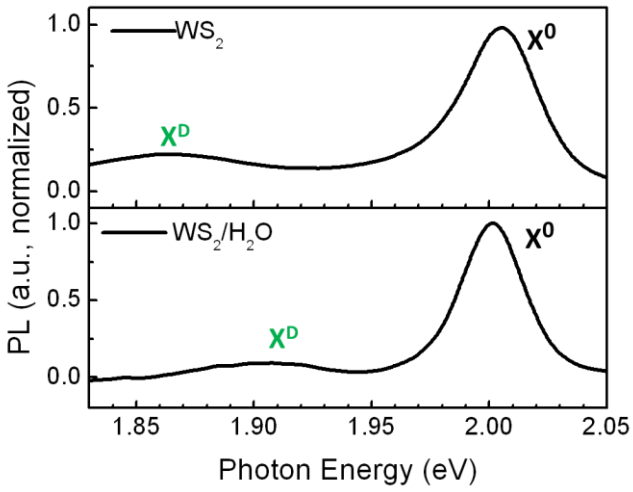

Figure 1.3. Photoluminescence spectra of TMDC (WS_2) in different environments. In both cases, monolayer WS_2 is deposited on SiO_2 substrate with the dielectric constant of ~3. However, dielectric constant of environment on top of WS_2 is different: 1 in the case of WS_2 device in air (top) and ~50 In the case of WS_2 device in water (bottom).

(A) Semimetals. Most prominent 2D semimetal is, of course, monolayer of graphite – graphene[6] – first 2D material ever discovered and studied. Due to low dimensionality, charge carrier density in graphene as well as in other 2D materials can be efficiently controlled through a process known as gating. Gating relies on inducing electric charges in a 2D material by using it as one of the plates of a parallel-plate capacitor. In this case, 2D material acts as a channel of a field-effect transistor. Graphene possesses highest electrical mobility >200 000$cm^2V^{-1}s^{-1}$[17] and even allows ballistic transport. Graphene also shows many other physical effects: presence of chiral effectively massless Dirac carriers, anomalous quantum hall effect (QHE)[18], fractional QHE[19], etc. Optically, graphene has relatively high, considering its 0.3nm thickness, absorption coefficient of $\pi\alpha\approx2.3\%$ [20], interestingly, tied to the fine structure constant α. Moreover, graphene has an excitonic feature, associated with a saddle point of the band structure[21], in the UV range. Despite having some unusual optical properties, absence of a bandgap in graphene does not allow to observe the full range of light-matter interactions possible in other 2D materials, like 2D semiconductors. Thus, graphene is mostly valued for its electrical transport properties.

(B) Semiconductors, such as 1L TMDCs have a large band gap of ~2eV conveniently located in the visible range of the optical spectrum. Unlike graphene, TMDCs have quite poor electrical properties characterized by mobility of <1000$cm^2V^{-1}s^{-1}$[22]. Although there does not seem to be any fundamental limitation on TMDC electrical transport properties, currently there is no well-established way of improving carrier mobility in TMDC. Nevertheless, as discussed above, 2D semiconductors display extremely rich excitonic physics and strong light-matter interactions.

(C) Insulators. Most common layered insulator with a bandgap of 5~6eV is hexagonal boron nitride hBN[23] which does have large electrical resistance of $10^{15}\Omega$cm[24] and even has excitonic features in the vacuum-UV range. Typically, hBN is treated as an auxiliary material used as an insulating spacer, tunneling barrier or gate dielectric.

(D) 0D materials. Some of the earliest discovered low-dimensional materials include zero-dimensional nanoparticles, such as Buckminsterfullerene C_{60}[25], plasmonic nanoparticles and quantum dots[26]. Quantum dots (QDs) are used in the current work as simplest two-level light-emitting/absorbing nanoparticles. Due to strong spatial confinement, QDs can host tightly bound excitons that emit or absorb light in the spectral range from infrared to ultraviolet. QDs can be used as energy donors or acceptors in the study of the simplest form of energy exchange between materials.

1.3. Interaction of low-dimensional materials with their environment

Along with electrostatic screening, described above, there are multiple other ways in which 2D materials can interact with their medium. Below we briefly discuss the most important mechanisms of interaction between 2D materials and their environments.

(A) Doping via charge transfer or band alignment. Nearby materials can strongly influence the carrier density of a 2D material. In one mechanism charges are transferred to the 2D material from impurities or molecules adsorbed on the 2D material itself[27,28] or on the substrate on which the 2D material is resting. Due to high surface-to-volume ratio, 2D material can be easily doped even without donor/acceptor ions being incorporated inside the material structure. Molecules or ions adsorbed on the surface can transfer charge to the 2D material and thereby significantly change its carrier

density. Alternatively, carrier density of a 2D material can be modified due to the band alignment between a 2D material and its substrate or, for example, metal electrode, covering the 2D crystal. A metal or a semiconductor placed on top[29] or underneath of the 2D material may have a significantly different workfunction than the 2D material itself. In that case the charges are transferred from the metal to the 2D material. As a result, the 2D material Fermi level can be altered by hundreds of meV. It is often possible to take advantage of these effects: by placing different materials on top of the 2D crystal or adsorbing donor or acceptor molecules on its surface, we can control material's Fermi level. This process is known as chemical doping. However, such doping effects cannot be precisely tuned and may lead to increased charge carrier scattering and other negative effects. For example, a substrate such as silicon dioxide, on which a 2D material rests in most of our devices has randomly charged dangling bonds and adsorbed ions. These surface modifications cause random fluctuations in the Fermi level of the 2D material. In many materials, such as MoS_2 and WS_2 upon fabrication, the Fermi level is originally located near the conduction band. As a result of the Fermi level fluctuations near the conduction band, random conducting and insulating regions are formed[30]. Such regions, also known as puddles, prevent continuous charge transport and cause additional scattering of charge carriers. Additionally, effects of charge transfer can affect excitonic and optical properties of TMDCs. Uncontrollable presence of free charge carriers can cause screening of e-h interactions by free electron gas and hence decrease exciton binding. Furthermore, free carriers occupy an area in the phase space of the 2D material and, due to Pauli exclusion principle, limit the amount of phase space available for the formation of an exciton.

This is a well-known phase space filling effect which tends to weaken e-h interactions and diminish optical intensities of excitons[31]. At the same time, charged defects or adsorbed ions allow us to observe new excitonic species. For example, defect-bound excitons (see Section 1.1) are observed in samples with naturally occurring or intentionally created charged impurities.

(B) Scattering. Presence of charged impurities and roughness of materials surrounding the monolayer crystal cause increased carrier scattering. Needless to say that it negatively affects electrical transport properties of 2D materials[17,27,28]. Moreover, excitons can also scatter off these impurities. This can trigger recombination or dissociation of excitons. Such effects can be removed by either making atomically-smooth substrates or by making suspended devices that are not in contact with any environment.

(C) Exchange processes. Two-dimensional materials can also interact with their environment via exchange of either charge or energy. These processes mostly affect excitons. The first process type is called Dexter electron transfer[32]. During this process a charge carrier from a 2D exciton gets transferred into the environment of a 2D material. This process of course limits exciton lifetimes. At the same time, the rate of such process drops exponentially quickly with distance separating exciton and its environment. This is related to the fact that charge transfer relies on tunneling. Other transfer process, called Forster resonant energy transfer (FRET)[33,34] is caused by near-field transfer of energy from an exciton to its environment and vice versa: e.g. exciton in a 2D material recombines by emitting a virtual photon that is immediately absorbed by the medium. Since this type of exchange is related to dipole-dipole interactions, its rate drops with distance polynomially – much slower than the Dexter

process. Naturally, FRET requires absorption and emission spectra of the interacting materials to overlap.

(D) Screening. In addition to the environmental screening described in section 1.1, free carriers *inside* a 2D material itself can also screen interparticle interactions. The density of these free carriers is directly related to doping or gating[9]. Again, screening can have both adverse and beneficial effects[35]. Environment or 2D material itself can strongly screen excitons lowering their binding energies and weakening excitonic features (Fig.1.3). On the other hand, screening can be thought of as a "handle" to control excitons.

1.4. Outline of the current work

First, in chapter 2 we will start investigating properties of pristine suspended TMDCs in vacuum that do not interact with any environment. In these samples we will demonstrate reduced doping and carrier scattering. Using our pristine samples we will show the binding energy of MoS_2 excitons to be above 560meV. Later such devices will be used as a reference point for analyzing more complex structures. We will also look at other exotic excitonic species in TMDCs, such as C-exciton and study mechanisms of exciton dissociation and photoconversion.

Then, in chapter 3 we will switch to perhaps the simplest type of interactions between excitons and environment: Forster resonant energy transfer. As mentioned above, this process involves "one-way" energy exchange between 2D excitons and quantum dots, which in our case model the environment. We will measure the rate of this exchange and show that it can be controlled by electrically gating the 2D material.

In chapter 4 we will switch to the more complex type of interactions discussed in this work: dynamic screening of excitons. In this case the medium acts as a mediator of interparticle interactions. We will focus on the case of screening by materials with strongly frequency-dependent dielectric functions. In this case the screening becomes “dynamic” and excitons can no longer be straightforwardly described using Schrodinger equations. We will develop new and simple theoretical approaches to dynamic screening of excitons and will test these approaches experimentally.

In chapter 5 we will describe measurement and sample preparation techniques that we used in our work along with the principles of operation of our experimental setup.

CHAPTER 2. EXCITONS IN SUBSTRATE-FREE MoS_2

2.1. Introduction

As mentioned in chapter 1, it is important to understand properties of excitons in intrinsic TMDCs not interacting with the environment. Only in comparison with properties of intrinsic TMDCs it is possible to understand effects of environment on 2D materials. Despite rapid progress in understanding the electronic and optical properties of intrinsic TMDCs[36], many important fundamental questions remain unanswered:

1) What types of excitons exist in TMDCs and what are their binding energies? While calculations predict a plethora of excitonic states with extremely large binding energies[11,37], experimental progress has been hampered by large broadening of the excitonic peaks in the available samples[37,38].

2) How do substrate-related effects perturb the intrinsic properties of monolayer TMDCs? Indeed, there are indications that the presence of a substrate can cause strong carrier scattering[39,40] and affect exciton energies through screening[16].

3) What are the photoconversion mechanisms in TMDC devices? Despite indications of efficient photoconversion[41,42], photodetection[42], and strong interest in employing TMDCs as solar cells[43], it is currently unclear how strongly-bound excitons in TMDCs dissociate and contribute to the photocurrent.

Moreover, strong light-matter interactions[41] make TMDCs excellent materials for ultrasensitive photodetectors[42] and energy harvesting devices[43].

2.2. Substrate-supported devices

Our experimental results are geared towards answering these questions. First, we eliminate substrate-related screening in TMDCs by fabricating free-standing and electrically contacted MoS_2, $MoSe_2$, and WSe_2 specimens. We then use photocurrent spectroscopy as a versatile tool for studying excitons and their dissociation mechanisms. In monolayer (1L) MoS_2, we have observed well-defined peaks at ~1.9 eV and ~2.1 eV ('A' and 'B') and a broad peak 'C' at ~2.9 eV. We attribute the peaks A and B to optical absorption by band-edge excitons, and the peak C to absorption by excitons associated with the van Hove singularity of MoS_2. Compared to previously reported optical absorption measurements of supported MoS_2[38], our photocurrent spectra exhibit sharp and isolated peaks with near-zero background between them, suggesting the absence of disorder-related midgap states. Our suspended devices allow us to obtain experimentally, for the first time, the lower bound of the binding energy of band-edge excitons of MoS_2, $E_{bind} \geq 570$ meV. Finally, we investigate the photoconversion and photogain mechanisms in monolayer TMDCs. By controlling the source-drain voltage, we observe different dissociation pathways for A/B- and C-excitonic states, demonstrate photogain of the order of 1000 with response times faster than 1 ms, and uncover the mechanism of this photogain. We also demonstrate the universality of our techniques by performing measurements on other materials, such as bi- and multi-layer MoS_2, monolayer $MoSe_2$ and monolayer WSe_2. Our results demonstrate, for the first time, that photocurrent spectroscopy is an efficient tool for probing single- and many-body states in pristine TMDCs and suggest the application of TMDCs as efficient photodetectors with a voltage-tunable spectral response.

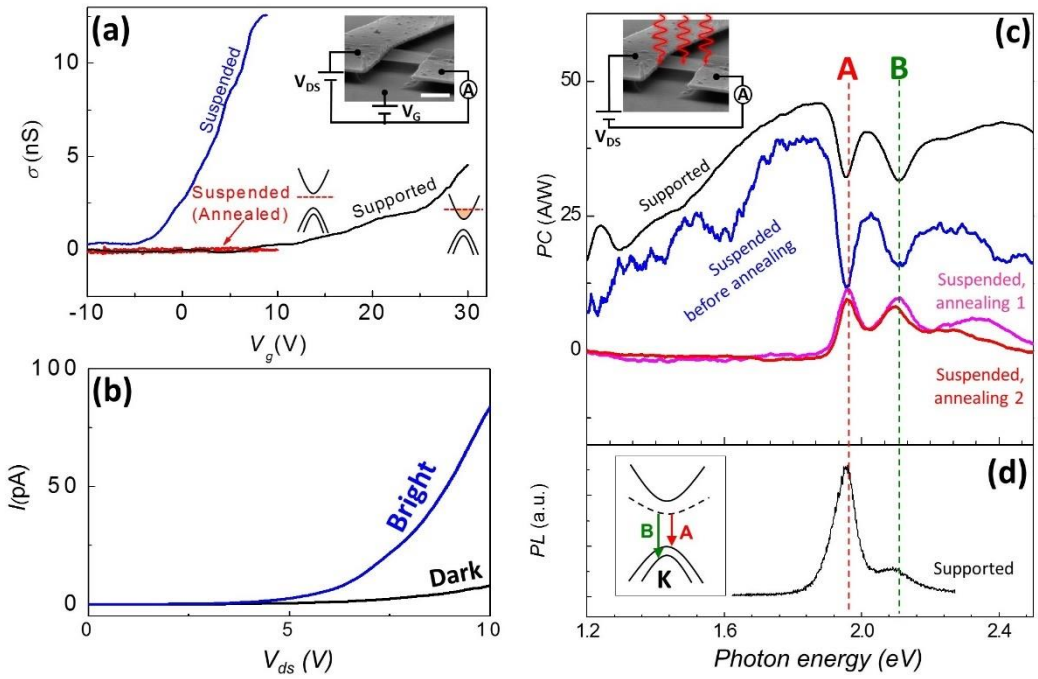

Figure 2.1. Effects of substrate and thermal annealing on conductance and photocurrent of suspended MoS_2. (a) Gate-dependent conductance of supported, suspended, and suspended annealed 1L-MoS_2 devices at T=300K. Inset: Image of the device. The scale bar is 1 μm. Schematically drawn band diagrams show the position of the Fermi level (red dashed line). **(b)** Dark and bright electrical response of an annealed suspended device at T=77K. Illumination intensity is ~3pW/μm^2 and wavelength is λ=430nm. **(c)** Photocurrent (PC) spectrum of a supported and suspended MoS_2 devices at different stages of thermal annealing at T=77K. **(d)** Photoluminescence spectra for a supported MoS_2 device at T=300K. Since PL spectra were recorded at room temperature, we manually blue-shift them by 150meV to allow comparison with PC spectra obtained at T=77K (see Supplementary Information, S5 for details). Inset: Bandstructure schematics of MoS_2 near K-point illustrating the origin of band-edge excitons. The dashed line represents excitonic states. Note that figures **a,c** were obtained using annealed device #1, whereas figure **b** was obtained using suspended device #2, which showed strong intrinsic photoresponse even without annealing.

2.3. Suspended devices.

In attempt to decrease the substrate-induced screening and disorder in TMDCs, we studied electrically contacted 14 suspended devices made from different TMDCs and of typical dimension ~1 μm×1 μm (see Supplementary information, S1 for details), following the approach developed for graphene[39]. Initially, we focus on 1L-MoS_2 devices (Fig. 2.1a, Inset), while discussing the case of monolayer $MoSe_2$, WSe_2, and multilayer MoS_2 later. Two-probe electrical transport measurements indicate that upon suspension the field effect carrier mobility (μ) of a typical device (device #1), ~0.05 cm^2/Vs, increases by an order of magnitude (Fig. 2.1a), consistent with a recent report[40]. We note that since neither the contact resistance nor the carrier density can be determined in the two-probe geometry, the physically relevant Hall or four-probe mobility of the same device may be larger by orders of magnitude[44-46]. To further increase the quality of suspended devices, we rely on thermal annealing, which is effective in improving μ both for graphene[39] and multilayer MoS_2[47]. Since the low electrical conductance (G) of MoS_2 devices precludes annealing via Ohmic heating[39], we instead locally heat the region of the wafer that is in thermal contact with the device. The annealing is performed *in situ* inside a cryostat kept at base temperature $T=77K$ using a ~5W CO_2 laser beam, which is defocused (intensity <20μW/μm^2) to avoid sample damage. Annealed and unannealed MoS_2 samples were imaged with atomic resolution using aberration-corrected scanning transmission electron microscopy. We did not observe any annealing-induced modification or defects (see Supplementary Information, S2). This annealing renders the device near-insulating under small source-drain bias voltage $|V_{ds}|<1V$ (Fig. 2.1a, red curve). This behavior is consistent with a pristine undoped semiconductor with the Fermi level located inside the band gap. Since the gate voltage is limited to $|V_g|<12V$ to avoid electrostatic

collapse of MoS_2, we are unable to achieve either electron or hole conductivity regimes via electrostatic gating.

To investigate suspended devices further, we measure PC under high V_{ds} *(>3*V*)* (Fig. 2.1b, blue curve). We illuminate the entire device using a low intensity (≤30 pW/μm^2) light source and record photocurrent I_{PC} across the device as a function of the photon energy $\hbar\omega$ (Fig. 2.1c). The total current through the device is $I=V_{ds}\ G(V_{ds}, n)$, where G in turn depends on the number of charge carriers n and V_{ds}. Upon illumination with power P, n increases by $\Delta n = (P/\hbar\omega)\alpha(\hbar\omega)D\tau$, where α is the absorption coefficient, D is the photoconversion probability (the probability of generating an unbound photocarrier by an absorbed photon), and τ is the photocarrier lifetime[48]. For a constant V_{ds}, the photocurrent is

$$I_{PC} = V_{ds}\frac{\partial G}{\partial n}\Delta n = \left[V_{ds}\frac{\partial G}{\partial n}\frac{D\tau}{e}\right]e\frac{P}{\hbar\omega}\alpha(\hbar\omega) \qquad (2.1),$$

where e is the electron charge. The expression inside the brackets is the photogain η, the ratio between the number of photocarriers transported across the device and the number of absorbed photons per unit time. We estimate η~200 at V_{ds}~10V, for a device #2. In other devices (device #3, Fig. 2.4b) η >1,000 (we assume that α(1.9eV)~0.1 and α(2.9eV)~0.4[38]).

Equation (2.1) is central to the analysis of our data as it shows that PC can be used to estimate the intrinsic parameters of TMDCs – $\alpha(\hbar\omega)$, τ, and D. Indeed, since the photogain is weakly wavelength-dependent, peaks in I_{PC} are associated with peaks in $\alpha(\hbar\omega)$ (See the

Supplementary Information, S4 for more detail). On the other hand, the amplitude of I_{PC} is related to photogain, and hence to D and τ. Therefore, similarly to optical absorption measurements, PC spectroscopy allows us to study single- and many-body electronic states in TMDCs[49,50]. Unlike absorption spectroscopy, PC can be easily measured for an electrically contacted microscopic device in a cryogenic environment, as the device itself acts as its own photodetector. Moreover, high photosensitivity of TMDC phototransistors allows us to use very low illumination intensity in our experiments, thereby excluding artifacts, such as photo-thermoelectric effects[51] (which would yield currents <0.1pA, more than three order of magnitude smaller than the photocurrent measured in our devices) and optically non-linear[52] effects arising at high photocarrier densities. We first use PC spectroscopy to probe absorption spectrum $\alpha(\hbar\omega)$ of TMDCs, while later investigating the origins of large photogain.

For substrate-supported and for majority of suspended unannealed devices, we observe two dips (similar dips were seen in photocurrent spectra of bulk TMDCs previously[53]) at ~1.9eV and ~2.1eV (Fig. 2.1c) on top of a largely featureless device-dependent background photocurrent attributable to absorption by midgap states[54] as well as to photogating artifacts[55,56] (detailed discussion is in the Supplementary Information, S3). Upon annealing, this background, attributable to absorption by midgap states[54] as well as to photogating artifacts[55,56] recedes leaving a set of universal features seen in every device. Photoconductivity spectrum of a high-quality device #2 is shown in Fig. 2.2a. We observe: (*i)* Two sharp peaks at ~1.9 eV and ~2.1 eV (labeled 'A' and 'B', respectively), *(ii)* near-zero PC signal below the A-peak, between A- and B-peaks and above the B-peak (from ~2.1 eV to ~2.5eV), *(iii)* steep growth of PC starting at ~2.5eV, and *(iv)* a broad

and strong peak ‘C’ at ~2.9eV. To the best of our knowledge, this is the first observation of the

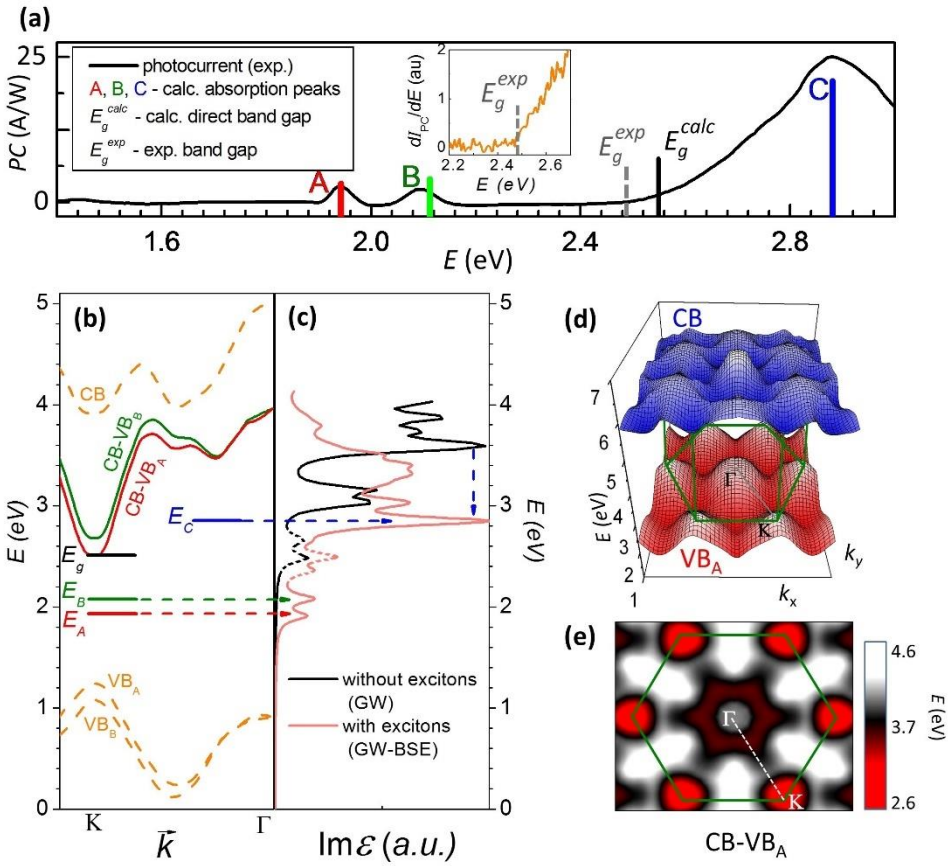

Figure 2.2. Probing excitons in pristine monolayer MoS_2 through photocurrent spectroscopy. (a) PC (V_{ds}=6V) spectrum of an intrinsic suspended 1L-MoS_2 device. Calculated positions of excitonic A-, B- and C-peaks and band gap E_g are shown as colored vertical bars. The bar height represents peaks amplitudes. The inset: derivative of the photocurrent plotted vs. the photon energy. Background photocurrent due the surface photovoltage of the substrate was subtracted from the data (see section S3 of the supplementary materials for details). **(b)** Electronic and optical band structures of 1L-MoS_2 along the K-Γ direction. The solid horizontal lines are the estimated positions of the excitonic bound states. **(c)** Optical spectrum of MoS_2 calculated with and without excitonic effects. The dashed peaks between 2.2 eV and 2.7 eV are computational artifacts, which are discussed in the Supplementary Information, S6. Vertical blue arrow indicates the position of the van Hove singularity downshifted by excitonic effects. **(d)** Three-dimensional plot of the band structure of MoS_2. **(e)** The colorplot of the optical band structure of MoS_2. Dark red gear shaped region around Γ is the local minimum corresponding to the excitonic C-peak.

features *(ii)-(iv)* in PC spectroscopy. Next, we demonstrate that all of these features originate from optical absorption by bound excitons as well as by unbound electron-hole (*e*-*h*) pairs in MoS_2.

Features A and B stem from optical absorption by the well-known[38,47,57] A- and B-band edge excitons of MoS_2 residing at *K*-points of the Brillouin zone (Fig. 2.1d, Inset). Recombination of these excitons results in photoluminescence peaks at similar spectral positions (Fig. 2.1d). The ~160 meV separation between the A- and B- peaks is a consequence of the splitting of the valence band of MoS_2 at the *K* point due to spin-orbit interactions[38,57,58]. The positions of the A- and B-peaks are also in good agreement with the calculated optical spectrum that we obtain using first-principles GW-BSE calculations (Fig. 2.2c, light-red curve,)[11,59-61]. See Supplementary Information, S6 for details.

The feature at ~2.9eV ('C') has been previously noted in absorption spectrum of MoS_2[38,47,59], but to the best of our knowledge not thoroughly analyzed. We interpret this peak as coming from an excitonic state associated with the van Hove singularity of 1L-MoS_2. This van Hove singularity is peculiar, as neither the conduction nor the valence bands have singularities in the density of states in the corresponding region of the Brillouin zone between *K* and Γ points (orange curves in Fig. 2.2b and Fig. 2.2d). At the same time, the bands are locally parallel in that region, causing a local minimum in the Mexican-hat-like *optical band structure* (difference between conduction and valence bands shown in Fig. 2.2b as red and green curves). This minimum is prominent in a 2D colorplot of the optical band structure as a continuous gear-shaped region circling the Γ point (Fig. 2.2e, dark red region). The large joint density of states associated with

this minimum yields a strong peak in $\alpha(\hbar\omega)$. Indeed, our GW calculations (*i.e.*, without inclusion of excitonic effects) of the optical spectrum prominently feature a sharp peak at ~3.45 eV, the value that corresponds to the optical band gap at the van Hove singularity point (Fig. 2.2c, black curve). Excitonic effects downshift the peak to ~2.9eV (Fig. 2.2c, light-red curve), very close to the experimentally measured position of the C-peak. Interestingly, the C-exciton valley of the optical bandstructure is near-rotationally symmetric rendering this exciton effectively one-dimensional[62]. Moreover, the location of the C-exciton at the bottom of the Mexican hat dispersion suggest that this exciton is localized in both real and momentum space, a conclusion also supported by first-principles calculations[37,59]..

Within the resolution of our measurements (signal-to-noise ratio is ~20 for A/B-peaks), we observe zero photocurrent below the A-peak, between the A- and B-peaks and between the B- and C-peaks. This observation is in contrast with non-zero optical absorption[38] and photocurrent in the same region in supported devices measured by us (data in the Supplementary Information, S4) as well as by others[38,47]. It has been previously suggested[63] and observed[47,64] that disorder-related midgap states can significantly perturb the optical response of MoS_2 leading to below-band gap absorption. Moreover, reduction in the background absorption upon annealing, which is likely associated with reduced disorder, has been recently observed in chemically exfoliated MoS_2 samples[47]. We therefore interpret the lack of PC background in our devices as a signature of the low density of the disorder-related midgap states. Moreover, we do not observe any features due to trions[65,66] and trapped excitons[64], which suggests that our devices are undoped and contain low defect density. We also note that despite the high quality of our devices, no signatures of anticipated[37,67] excited states of A or B excitons are observed. This is

consistent with the very low oscillator strength of these states expected from a simple 2D hydrogen model (see Supplementary Information, S7).

Above the near-zero photocurrent region, we observe a featureless and abrupt increase of the PC above E_g^{exp} ~2.5 eV. This increase is clearly visible in the plot of $dI_{PC}/d(\hbar\omega)$ (Fig. 2.2a, Inset). The PC onset occurs very close in energy to the calculated *fundamental* (i.e. single-particle) band gap of 1L-MoS_2, E_g^{calc} ~2.55 eV (Fig. 2.2b-c) and is therefore related to direct band-to-band absorption by unbound *e-h* pairs. However, experimentally we cannot distinguish the onset of the band-to-band absorption from the tail of the C-peak. We therefore interpret that the measured value of E_g is a lower bound for the fundamental band gap value. We can therefore *experimentally* estimate the exciton binding energy in MoS_2 as $E_{bind}=E_g-E_A \geq 570$ meV. We emphasize that in our suspended devices the measured values for E_g and E_{bind} are free from the influence of the substrate-related dielectric screening and hence can be directly compared to calculations (Fig. 2.2a-c).

2.4. Other types of 2D semiconductors

We now turn to bi- and multi-layer MoS_2, as well as other 1L-TMDCs, such as $MoSe_2$ and WSe_2. Similar A-, B-, and C- features are seen in photocurrent spectra for all of these materials (Fig. 2.3a). For materials other than 1L-MoS_2, however, we do not observe the zero photocurrent between B- and C-peaks. This precludes direct experimental estimation of exciton binding energies in these materials. However, since our first-principles calculations of E_g, A-, B- and C-peaks for 1L MoS_2 are in good agreement with the experimental data, we can infer E_g and E_{bind} of other TMDC materials from corresponding A-, B- and C-peak positions (details are in Supplementary Information, S6). We note the following trends:

(i) The A- and B- peaks in MoS_2 do not depend significantly on its thickness (Fig. 2.3b, red points)[38]. This is a consequence of simultaneous and nearly equal reduction of E_g (Fig. 2.3b, black points) and E_{bind} with the number of layers of MoS_2[68].

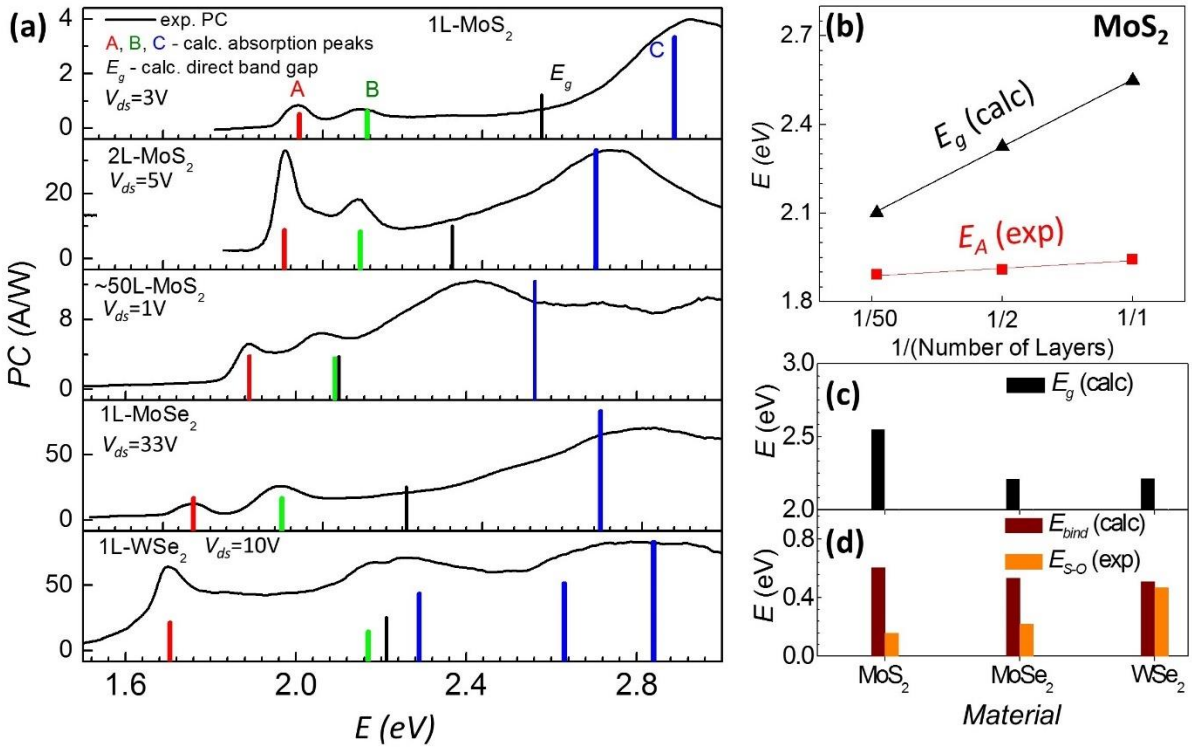

Figure 2.3. Photocurrent in various TMDC materials. (a) Experimental PC spectra of different TMDC devices. Solid bars are calculated excitonic peaks and band gap values. The top panel shows the PC spectra of an annealed 1L MoS_2 device (device#3). Large spin-orbit coupling of WSe_2 results in splitting of the valence and the conduction bands even near Γ-point, which leads to splitting of the C-peak. All the devices are suspended and annealed except for the multilayer MoS_2 device, which is supported on a glass substrate (see Supplementary Information, S1). For each device, the bias voltage was chosen to maximize signal to noise ratio for the photocurrent. **(b)** Dependence of excitonic peak positions and band gap values on number of layers of MoS_2. **(c,d)** Comparison of E_g, E_{bind} and spin-orbit coupling strengths for different 1L-TMDCs.

(ii) The splitting between A and B peaks is largest in WSe_2 (~510 meV), followed by $MoSe_2$ and MoS_2 (Fig. 2.3d). This is a signature of the stronger spin-orbit interaction in WSe_2, related to the higher atomic number of tungsten.

*(iii)*The calculations suggest that variation of the type of chalcogen (S, Se) atom has a strong effect on E_g (Fig. 2.3c). This is a consequence of the dependence of the lattice constant on the type of chalcogen atoms. On the other hand, E_{bind} remains roughly constant for all measured materials (Fig. 2.3d).

2.5. Exciton dissociation and photocurrent generation mechanisms

Our next aim is to understand very large PC magnitude. To contribute to photocurrent, a neutral exciton must first dissociate into an unbound electron-hole pair. This process is characterized by the probability D entering into Eq. (1).To investigate the mechanism of dissociation in 1L-MoS_2, we examine I_{PC} *vs.* V_{ds}. We find that the A and B peaks in the photocurrent practically disappear at low V_{ds}, while the C peak remains prominent (Fig. 2.4a). This behavior is consistent with dissociation of excitons by strong electric fields arising near the interface between MoS_2 and metallic contacts. Indeed, a large electric field is required to overcome the binding energy $E_{bind} \geq 0.6$ eV for A-excitons. Such a field can arise at the interface between MoS_2 and a metallic contact due to the application of a large bias voltage (like in the case of pristine organic semiconductors[69]) and possibly due to the mismatch of the work functions of MoS_2 and metal (similar to nanotube devices[70] and excitonic solar cells[71]). Our conclusion that PC is produced only at the contacts is also supported by scanning photocurrent microscopy measurements directly mapping photocurrent production[72]. In contrast, C-excitons exist above

the band gap and therefore can produce unbound *e-h* pair even without application of an external electric field. Thus we demonstrate for the first time electric field assisted dissociation of A- and B-excitons and spontaneous decay of C-excitons into a free electron-hole pairs.

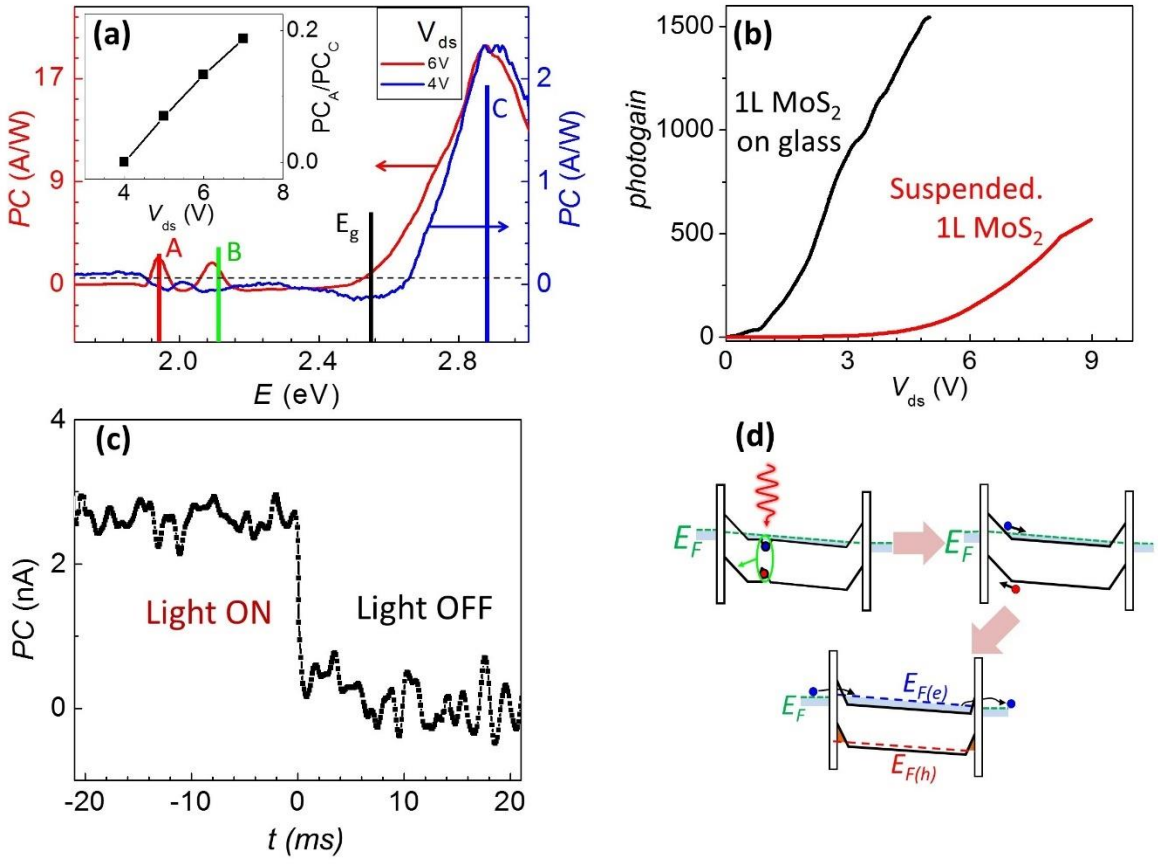

Figure 2.4. Photoconversion mechanisms in monolayer MoS_2. (a) PC spectra measured in a suspended 1L-MoS_2 at two different V_{ds}. Both curves are normalized to the height of the C-peak. Inset: relative PC amplitudes of A- and C- peaks *vs.* V_{ds}. Note that apparent negative photocurrent around ~2.5eV is an artifact caused by our procedure for background subtraction (see Supplementary Information, S3). **(b)** Photogain for a glass-supported and suspended devices *vs.* V_{ds}. The device is illuminated at λ=640nm with intensity~30 pW/μm^2. **(c)** Time response of PC to the varying light intensity in a glass-supported MoS_2. This measurements sets the upper limit for the response time <1ms. Accuracy of time-resolved measurements was limited by the high resistance of MoS_2 and therefore high RC-time constant of the measurement circuit. **(d)** Schematics (not to scale) of the photogain mechanism. E_F, $E_{F(e)}$ and $E_{F(h)}$ represents the Fermi level, elelctron quasi-Fermi level and hole quasi-Fermi level, respectively.

Finally, we analyze the reason for the very large photogain (η > 1,000) and photoresponsivity (~50 A/W) in our devices (Fig. 2.4b). We note that very different values of photoresponsivity has been reported in literature from 1 mA/W [72],[73] to 880 A/W[42] for monolayer MoS_2 and from 5mA/W[72] to 0.57 A/W for multilayer MoS_2[74]. Previously suggested mechanisms, such as the direct dissociation at the contacts (yielding only η < 1)[72] or photothermoelectric effect (yielding $\eta << 0.1$)[51] cannot explain very high observed photogain. Generally, large gain can be related either to multiplication of photocarriers due to the avalanche effect[48], or to a long photocarrier lifetime τ due to the trapping of photoexcited carriers either in the defect states (persistent photoconductivity[48]) or in the band-bending region between a metal contact and a semiconductor[75]. However, as mentioned above, clean suspended MoS_2 devices only start to conduct ($G \sim 10^{-7}$ S) at large ($V_{ds}>E_g/e$) source-drain bias (Fig. 2.1b). Operation in this regime may be complicated by additional effects, such as Zener or thermal breakdown[75]. On the other hand, we observe that glass-supported MoS_2 devices (chosen to eliminate parasitic photogating) have dark conductance $G\sim10^{-5}$ S, likely due to the higher doping level of supported MoS_2. In agreement with Eq. (1), the photoresponse of these devices is correspondingly higher and can be observed even at small V_{ds} (Fig. 2.4b). Moreover, the relatively low resistance and correspondingly low RC time-constant of glass-supported devices allows us to measure the time dependence of the photocurrent.

The observation of $\eta\sim25$ at $V_{ds}\sim0.5$ V for a glass-supported device (Fig. 2.4b) rules out the avalanche effect as the mechanism responsible for the observed high photogain. In this regime, the energy eV_{ds} is well below the fundamental band gap and is not sufficient to start an avalanche. Persistent photoconductivity has been previously reported in MoS_2[42], but we can exclude it as a

possible candidate for the PC generation in clean MoS_2 because we routinely observe characteristic photoresponse time <1 ms at low temperatures (Fig. 2.4c). This is approximately five orders of magnitude faster than the response time reported for persistent photoconductivity[42], but still slower compared to the carrier transit time (time it takes a carrier to travel across the device). The large photogain of our devices is most consistent with photocarrier trapping mechanism also seen in metal-semiconductor-metal and tunnel-emitter phototransistors[75]. Upon illumination, photoexcited holes are trapped in the potential well formed due to band bending[76] at the interface between MoS_2 and Au metallic contacts. At the same time, the electrons are injected into the MoS_2 channel (Fig. 2.4d). According to the Eq. 1 this leads to very large changes in the photoconductivity. First, spatial separation of photocarriers precludes their recombination and greatly increases their lifetime τ. Second, high concentration of holes near the metal-semiconductor junction decreases the thickness of the Schottky barrier and reduces contact resistance[75].

2.6. Conclusions

In conclusion, we note several potential applications of the obtained results. First, the large photogain, fast photoresponse, and bias-voltage dependence of the photocurrent spectra of pristine monolayer TMDCs suggest applications of these materials as sensitive and voltage-tunable photodetectors[77]. Second, the high absorption and dissociation probability of C-excitons may be employed in creating efficient TMDC-based solar cells[43,78]. Finally, observed effects of suspension and annealing on electronical and optoelectronical properties of our devices pose multiple questions regarding intrinsic and extrinsic properties of TMDC devices: effects of substrate, screening, intrinsic doping, intrinsic mobility, etc[36].

While our manuscript was under review, several groups also reported experimental measurements of the binding energy for excitons in 1L TMDCs ~300-700 meV[79-81], which is very close to the estimate obtained here. Two groups also reported lower exciton binding energy ~350 meV[82,83] in 1L on substrate and predict ~500 meV in vacuum[79,82].

CHAPTER 3. ENERGY EXCHANGE BETWEEN 2D EXCITONS AND QUANTUM DOT ENVIRONMENT

3.1. Introduction

In this chapter we use quantum dots (QDs) as a proxy environment to model the simplest "one-way" type of exchange-interaction between 2D materials and their surrounding. We take advantage of the fact that quantum dots and fluorophores, like other anoscale emitters, strongly interact with materials located in their close proximity. An optical excitation in a QD can be transferred into the environment non-radiatively via processes such as charge transfer and Förster resonant energy transfer (FRET). These types of interaction are directed from one sub-system to another. Unlike the Dexter transfer discussed in chapter 1, FRET is a very efficent long-range optical process[84]. This type of energy transfer can be viewed as a simple test bed for observing interactions between excitons in 2D material and their environment: it is a one-way process in which one subsystems gives its energy to the other. As mentioned in chapter 1, due to atomic thickness of 2D matrials, their optical parameters can be controlled via electrostatic gating[85-88]. From the practical point of view, this enables electrical control of FRET and leads to potential applications of controllable nanoemitters. We therefore expect that by placing a nanoemitter onto a 2D material, it may be possible to observe QD-exciton interactions and electrically control the FRET pathway between the two systems.

Specifically, we explore FRET between chemically synthesized QDs and two-dimensional semiconductor (2DSC) monolayer molybdenum disulfide (MoS_2).[89,90] FRET in such a system is especially interesting due to the presence of tightly bound excitons in MoS_2 that are stable at room temperature.[59,91-93] Moreover, the oscillator strength of these excitons is strongly

modified by the presence of the charge carries in MoS_2.[85-87] We find strong quenching of photoluminescence (PL) for QDs near MoS_2, demonstrate that this quenching is due to FRET between QDs and excitons in MoS_2, and prove that other mechanisms such as charge transfer do not play a role in this system. Furthermore, we observe ~75% modulation of QD photoluminescence intensity with electrostatic gating of MoS_2. We find that this phenomenon is caused by ~500% electrical modulation of the QD/MoS_2 FRET rate. This, in turn, is caused by changes in the near-field absorption of MoS_2 related to interaction of MoS_2 excitons with free charge carriers.

Very recently, related approaches have been demonstrated to achieve electrical control of the FRET rate for QDs and other nanoscale infrared emitters near another 2D material, graphene.[94,95] Our use of 2DSC offers several distinct advantages. The sizeable bandgaps of 2DSCs allow us to achieve electrical modulation of FRET from QDs emitting in the visible range. The strong electrical modulation of excitons in 2DSCs allows for the operation of devices with significantly reduced electrical fields, compared to graphene. Finally, we show selective modulation of QDs at desired wavelengths by choosing 2DSCs with corresponding excitonic features.[96]

3.2. FRET between QDs and two-dimensional semiconductors

To explore near-field energy transfer between QDs and 2DSCs, it is important to understand the condition under which such transfer is expected. In general, FRET between two systems depends on their separation distance and the overlap integral between the absorption and emission spectra. The Fermi golden rule yields the following estimate for the FRET rate between a 0D and a 2D system (details in Supporting Information, S1):[84,97,98]

$$k_{FRET} \sim \frac{1}{d^4} \int_0^\infty \alpha(\lambda) f(\lambda) \lambda^4 d\lambda. \quad (3.1)$$

In this expression $f(\lambda)$ is the normalized emission of QDs, $\alpha(\lambda)$ is the absorption coefficient for a 2DSC as a function of wavelength λ, and d is the distance between QDs and a 2DSC. The peculiar d^{-4} dependence of k_{FRET} is a characteristic of near-field coupling between excitations in 0D and 2D systems.[84,98] Equation (3.1) indicates that in order to observe large k_{FRET}, the following conditions must be satisfied: *(i)* The optical absorption of the 2DSC must be sizable at the QD emission wavelength. *(ii)* A small QD/2DSC separation d and a large spectral overlap between the QD emission $f(\lambda)$ and 2DSC absorption $\alpha(\lambda)$ is needed to achieve a large transfer rate. *(iii)* The lifetime of an exciton in QDs, τ_{QD}, must be longer than the inverse rate of energy transfer, k_{FRET}^{-1}. When this condition is fulfilled, an exciton in a QD lives long enough to transfer its energy into a 2DSC.

We can now select the appropriate materials to observe and explore FRET between QDs and 2DSCs. From the diverse group of 2DSCs (*e.g.*: MoS_2, WSe_2, WS_2), we chose monolayer MoS_2, a direct band gap semiconductor that is well studied, readily available, and optically active in the visible range.[89,90] The absorption spectrum of MoS_2 (Fig. 3.1a) is dominated by two strong excitonic PL peaks at 1.88eV (A) and 2.05eV (B). These features are due to absorption of light by tightly bound band-edge A- and B-excitons[59,91-93] residing at the K-point of the Brillouin zone (Fig. 3.1a, inset). The energy separation between the excitons is due to strong spin-orbit interaction[59] that splits the valence band of MoS_2. The photoluminescence spectrum of MoS_2 is dominated by A-excitons, the lowest excited state (Fig. 3.1b). With increased electron doping, both absorption (Fig. 3.1a, dashed line) and photoluminescence (Fig. 3.1b, dashed line) of MoS_2 are strongly reduced for energies corresponding to A- and B-peaks. This strong electro-

optical effect is related to the interaction between excitons and free charge carriers in MoS_2. Doping-induced reduction of absorption is attributed to a combination of phase-space filling effect (blocking of low-momentum states that are needed for exciton formation) and screening of electron-hole interactions by free carriers.[99,100] Additionally, doping allows the formation of charged excitons (trions),[86,87] that become the new lowest-energy excitonic state and hence modify the PL spectrum.

We chose compositionally graded alloy core-shell CdSSe QDs[101] as the emission source. The QDs were synthesized to emit at ~2.05eV (Fig. 3.1c), very close to the B-peak in the absorption spectrum of MoS_2 (Fig. 3.1a). Additionally, CdSSe QDs are very bright (quantum yield ~50%) and have lifetimes ~3ns (Fig. 3.1c, Inset). This is much longer than the ~8ps lifetime of excitons in MoS_2 (Fig. 3.1b, Inset; see "Methods" for measurement details). This ensures that FRET will be directed from QDs to MoS_2.[102,103] Due to the spectral separation between the PL peaks of QDs and MoS_2, their spectra can be analyzed independently in hybrid structures.

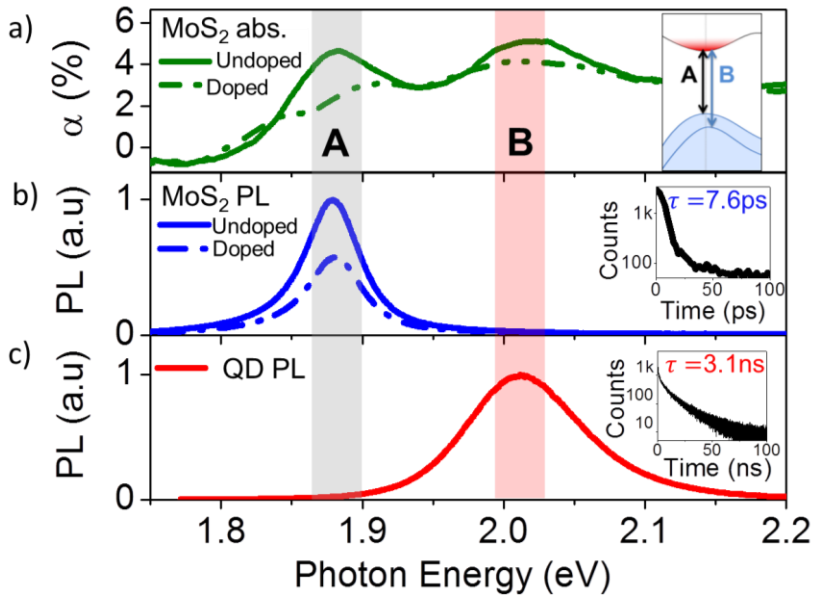

Figure 3. 2. (a) Absorption spectra of monolayer MoS_2 at two different doping levels. Inset: bandstructure of MoS_2 near its K-point. **(b)** PL spectra of monolayer MoS_2 at two different doping levels. Inset: time-resolved PL due to A-excitons in MoS_2. **(c)** PL spectrum of CdSSe QDs. Inset: time-resolved PL of excitons in QDs.

Having spectrally satisfied FRET conditions in our hybrid structures, the next step is to physically bring QDs and a 2DSC in close proximity. We developed a flexible approach to address the biggest challenge in such devices – fabrication of uniform monolayer films of QDs. First, we used chemical self-assembly to deposit a uniform layer of QDs onto a SiO_2 substrate. The SiO_2 substrate functionalized with (3-Mercaptopropyl) trimethoxysilane was submerged into a solution of oleic acid-ligated CdSSe QDs (Fig. 3.2a, see "Methods" for details).[104] The exposed thiol groups displace the oleic acid surface ligands and bind the QDs to the substrate.[105] The density of QDs was optimized to produce sub-monolayer films such that PL peaks due to QDs and MoS_2 could be distinguished. We used PL spectroscopy and atomic force microscopy (AFM) to assess the uniformity of QD films. With AFM we determined that the thickness of the QD film is ~7nm (Fig. 3.2b, Inset). This thickness is consistent with a sub-monolayer film of QDs that are ~5nm in diameter and have 1-2nm long oleic acid ligands.[106] Photoluminescence imaging indicates that as-fabricated QD films remain bright and are very uniform (Fig. 3.2b). Moreover, the position and the width of the PL peak for the QD film (Fig. 3.2c, red line) do not differ significantly from that of same QDs in solution (Fig. 3.2c, black dotted line). This suggests that the QDs are not chemically modified during the process of self-assembly and that the interactions between QDs are negligible. Each QD in the film can therefore be treated as a single emitter.

Finally, we mechanically transferred a monolayer MoS_2 onto QDs using fabrication techniques developed for 2D heterostructures.[107,108] Several experimental tests described below confirm that such transfer does not perturb the QD layer.

3.3. Results and Discussion

Experimental evidence of FRET

A typical sample along with its optical and PL image is shown in Fig. 3.3a. This sample can be considered ungated ($V_g=0$) compared to electrostatically gated devices studied further. Both the PL image and PL spectra (Fig. 3.3a,b) indicate strong suppression of photoluminescence for the QDs that are close to MoS_2. To quantify this effect, we introduce the quenching factor $Q = I_{QD}/I_{QD/MoS_2}$. Here I_{QD/MoS_2} is the height of the QD photoluminescence peak at 2.05eV for the hybrid QD/MoS_2 device (acquired at a point marked red in Fig. 3.3a), and I_{QD} is the height of the same peak from QDs away from MoS_2 (acquired at a point marked black in Fig. 3.3a). We calculate $Q(0V)\sim 4.8$ from the data shown in Fig. 3.3b. We also observed that the lifetimes of QDs reduce by a similar amount due to the presence of MoS_2, $\tau_{QD}/\tau_{QD/MoS_2}\sim 4.4$ (Fig. 3.3b, Inset). At the same time, the position of the PL peak due to QDs remained virtually unchanged at about ~2.05eV (Fig. 3.3b). This indicates that the QDs are not chemically or mechanically perturbed by MoS_2.

The quenched PL and decreased lifetimes indicate the opening of an additional non-radiative relaxation channel for the QDs next to MoS_2. We attribute this pathway to FRET. Strong spectral overlap between the emission spectrum of QDs and B-peak in absorption of MoS_2 coupled with very small QD/MoS_2 separation should, according to Eq. (1), lead to large k_{FRET}. Prior experiments on similar QDs next to 2D systems (graphene, MoS_2) arrived at a similar conclusion.[109,110]

We confirmed that mechanisms other than FRET are not responsible for observed changes in PL in our devices. In principle, charge transfer between QDs and MoS_2 can also lead to non-radiative relaxation.[111-113] For our experiments we intentionally chose core-shell QDs with strong electron-hole pair confinement and long ligands.[106] Charge transfer in such core-shell QDs is likely inefficient or absent.[114] To further exclude the contribution of charge transfer, we fabricated devices with a spacer layer (5-15nm of SiO_2) inserted between QDs and MoS_2. Despite large MoS_2/QD separation, we observed significant quenching in PL of QDs atop of MoS_2 (Supporting Information, S2). Such quenching can only be attributed to long-range FRET, as short-range charge transfer should be fully suppressed in spacer devices. In addition, charge transfer is conclusively ruled by the optoelectronic measurements described in the last section of the manuscript. It is also feasible that dielectric screening due to MoS_2 could affect the intensity of QD photoluminescence. To exclude this possibility, we fabricated devices where hBN, an optically transparent insulator, is transferred onto QDs instead of MoS_2. While hBN has a dielectric constant ε 4~7, [115] similar to that of monolayer MoS_2,[116] we did not observe any spectral changes or quenching for QDs in hBN/QD devices. This confirms that the QDs are not affected by dielectric

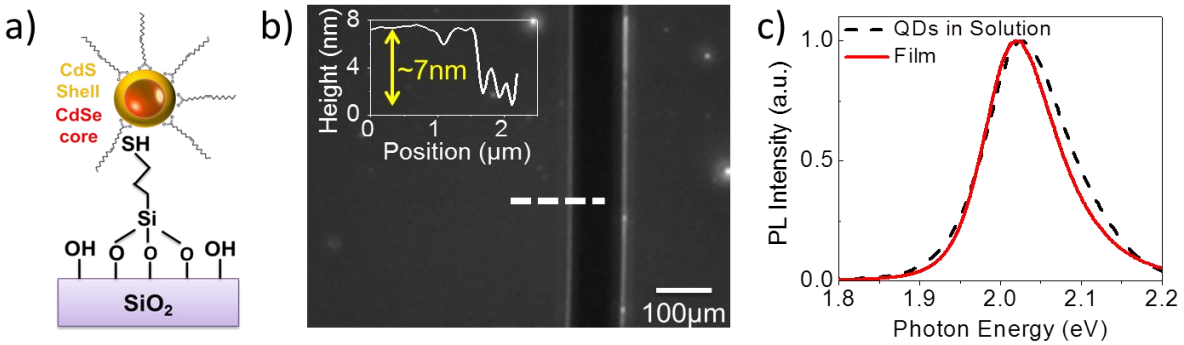

Figure 3.2. (a) CdSSe QDs with oleic acid ligands attached to functionalized SiO_2. **(b)** PL image of a QD film. A striation made on the film is evident as a dark strip. Inset: AFM height profile of the film obtained along the white dashed line in (b). **(c)** Normalized PL spectra of a QD film on SiO_2 and of the same QDs in solution.

screening due to neighboring materials. This also rules out the possibility of mechanical or chemical changes to the QD layer during the transfer procedure (Supporting Information, S3).

The QD/MoS_2 FRET rate was estimated from measured suppression of QD PL and lifetimes. The intensity of QD photoluminescence depends on radiative (k_r) and non-radiative (k_{nr},k_{FRET}) decay rates:

$$I_{QD} \sim \frac{k_r}{k_r + k_{nr}} = k_r \tau_{QD},$$

$$I_{QD/MoS_2} \sim \frac{k_r}{k_r + k_{nr} + k_{FRET}} = k_r \tau_{QD/MoS_2}. \quad (3.2)$$

In these equations, the lifetime of a QD is expressed as an inverse of the sum of radiative and non-radiative rates, and k_r is assumed to be unaffected by the environment. Equation (3.2) confirms that near-equal suppression of QD lifetime and PL intensity observed in our experiments is an expected consequence of FRET. From the measured PL quenching Q, using equation (3.2) we determined $k_{FRET} = (Q-1)/\tau_{QD} \sim (1.1 \pm 0.2) \times 10^9 s^{-1}$. Importantly, this rate corresponds to

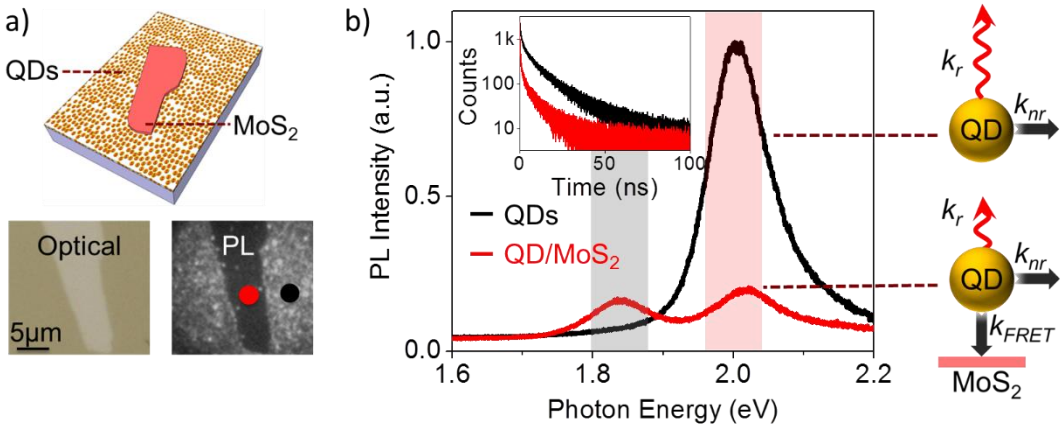

Figure 3.3. (a) Ungated MoS_2/QD device along with its optical (left) and photoluminescence (right) images. PL image was recorded using a band-pass filter (605nm-615nm) only transmitting QD emission. **(b)** PL spectra and time-resolved PL (Inset) of QD/MoS_2 hybrid (red) and of bare QD film (black). The spectra were recorded from the same device shown in Fig. 3.3a at positions marked by red and black circles. The schematic on the right illustrates FRET between a QD and MoS_2.

lifetime ~1ns, shorter than the intrinsic QD lifetime of ~3ns. Using $Q \sim 4.8$ and separation distance between QD-core and MoS_2 ~3.5nm (Fig. 3.2b inset), we evaluate FRET radius $R_0 \sim 5$nm.

3.4. Electrical modulation of FRET

Finally, we examined gate-induced modification of the optical properties of QD/MoS_2 devices. To enable such a study, we used fabrication described previously, but MoS_2 was transferred on top of pre-patterned gold electrodes. An optically transparent solid electrolyte was then deposited onto MoS_2 (Fig. 3.4a, see "Methods" for details). This configuration allows us to vary the carrier density inside MoS_2 while being able to perform optical measurements. It is also important to note that electric field is near-absent at the location of QDs and cannot affect their photoluminescence directly. Although very high carrier densities, $n \sim 10^{14}$ cm^{-2}, can be reached with electrolyte gates (Supporting Information, S4),[117] our devices require much smaller densities, $n \sim 10^{13}$ cm^{-2}, and efficiently operate at low gate voltages ($-2V < V_g < 2V$). Overall, we fabricated and measured 4 devices including the representative device shown in Fig. 3.4a.

With increased electron doping (positive V_g), we observed a well-known suppression of the PL peak[85,86] due to MoS_2 at 1.88eV as discussed earlier (Fig. 3.1b and Supporting Information Fig. 3.S4b). On the other hand, photoluminescence of QDs at ~2.05eV strongly increases with V_g (Fig. 3.4b). In our best device, we observed up to ~75% modulation of the QD photoluminescence intensity for V_g between -2V and 2V. This effect is reproducible for all measured devices and is stable over multiple sweeps of V_g (Fig. 3.4b, Inset).

We attribute the modulation of PL to gate-induced modulation of the FRET rate k_{FRET}. Indeed, as discussed above, optical absorption $\alpha(\lambda)$ of MoS_2 is strongly changing with V_g at $2.05eV$, the energy corresponding to QD emission (Fig. 3.1c). According to the equation (3.1), changes in $\alpha(\lambda)$ should lead to modulation of the FRET rate, and hence QD PL intensity.

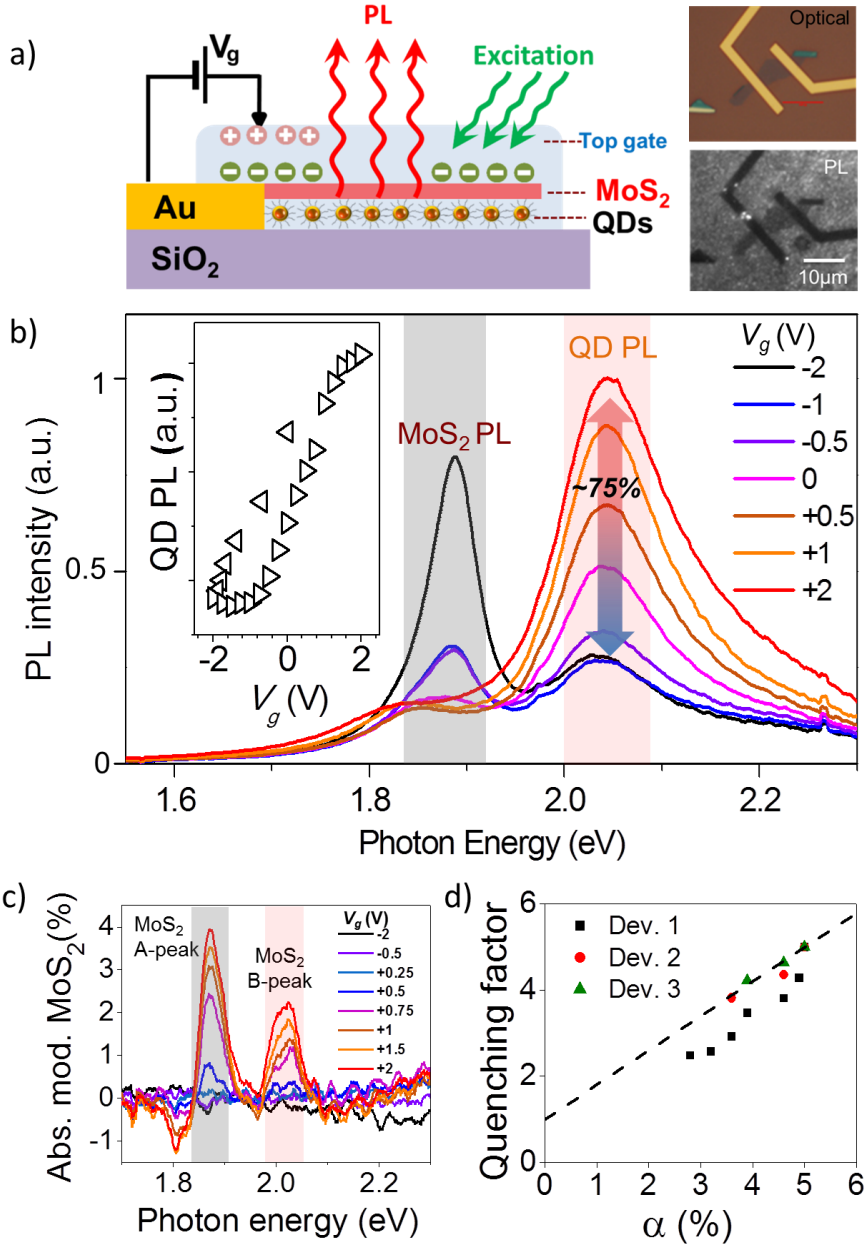

Figure 3.4. (a) Device schematic of electrolyte gated QD/MoS_2 hybrid. Optical and photoluminescence images of an electrically contacted QD/MoS_2 device. **(b)** PL spectra of a QD/MoS_2 device at different V_g. Inset: QD photoluminescence intensity vs. V_g during a back-and-forth sweep between +2V and -2V. **(c)** Transmittance modulation of MoS_2 The dip at ~1.8eV is likely related to charged exciton absorption. **(d)** From the measured Q vs. V_g from (a) and α vs. V_g from (b), a single parametric Q(α) plot was created. Since the transmission of MoS_2 is only reliably determined for V_g>0, only these points were used in the plot (details in Supporting Information, S6).

Our next goal is to understand the relationship between FRET modulation and MoS_2 absorption. In a separate measurement on a device without a QD layer, we used confocal transmission microscopy to record gate-induced transmittance modulation of MoS_2 defined as

$M = \left(I(\hbar\omega,\ V_g) - I(\hbar\omega,\ 0V)\right)/I(\hbar\omega,\ 0V)$. Here $I(\hbar\omega, V_g)$ is the intensity of light transmitted through MoS_2 at photon energy $\hbar\omega$ and gate voltage V_g. We use transmittance modulation as a proxy measurement for far-field absorption which is otherwise hard to access via conventional differential reflectivity measurements for our device geometry. A simple estimate yields $\alpha(V_g) = \alpha(0V) - M(V_g)$ (Details in Methods and Supporting Information, S5). Within our gating range we observe only ~2% modulation of MoS_2 transmittance at ~2.05eV (Fig. 3.4c), much smaller than ~75% modulation in QD photoluminescence.

We devised a simple model relating near-field FRET rate and quenching factor to far-field absorption of MoS_2. The normalized emission spectrum of an individual QD centered at wavelength λ is narrow compared to the relatively broad absorption features of MoS_2.[118] In this situation, equation (3.1) can be simplified to

$$k_{FRET} \sim \frac{1}{d^4}\alpha(\lambda, V_g).$$

Combining this with equation (3.2), we obtain the following expression for the quenching factor Q:

$$Q\ (\lambda, V_g) = \frac{\tau_{QD}}{\tau_{QD/MoS_2}} = 1 + \tau_{QD}k_{FRET} = 1 + A\alpha(\lambda, V_g). \quad (3.3)$$

Here $A \sim \frac{\tau_{QD}}{d^4}$ is a proportionality constant relating the quenching factor to absorption of MoS_2. From experimentally measured $Q(V_g=0) \sim 5$ (Fig. 3.3b) and $\alpha(V_g=0) \sim 5\%$ (Fig. 3.1b) at

λ=610nm (QD emission peak), we find $A = (Q(0) - 1)/\alpha(0) \sim 80$. The large value of A translates to large electrical modulation of PL of the QDs. To check the validity of our model, we plotted experimentally acquired values of Q and α. The measured $Q(\alpha)$ along with the prediction of equation (3.3) (dashed line) are plotted in Fig. 3.4d. The agreement between the experimental data and our model confirms that the observed modulation of QD photoluminescence is a consequence of electrical modulation of FRET. From Fig. 3.4b (inset) and equation (3.3) we also find that the FRET rate changes from $2.8\times10^{9}\mathrm{s}^{-1}$ to $0.5\times10^{9}\mathrm{s}^{-1}$ within our gating range.

We devised additional control experiments to further confirm that the observed PL modulation is related to gate-induced changes in excitonic absorption of two-dimensional semiconductors and not to other mechanisms. We fabricated one device where MoS_2 is substituted by a monolayer of graphene and another QD/MoS_2 device with different CdSSe QDs emitting at ~2.2eV, not in resonance with MoS_2 absorption peaks. In contrast to the devices discussed above (e.g. in Fig. 3.4a), in both of these samples optical absorption of the 2D material is gate-independent at the QD emission wavelength (Fig. 3.4c and Supporting Information, S7). As expected, since FRET modulation is spectrally selective, we did not observe any gate-dependent changes of the QD photoluminescence in either device in the range of gate voltage between -3V and 3V. Finally, we fabricated a device with QDs emitting at ~2.4eV, but with a different 2DSC, WS_2, instead of MoS_2. Large and clear modulation of QD PL is observed in this device since the gate-dependent excitonic peaks of WS_2 (A-peak: 2.0eV, B-peak: 2.4eV)[119] are in resonance with the QD emission peak (Supporting Information, S8).

These observations confirm that PL of QDs is only affected by the absorbance of a 2D material at relevant frequencies and not just its carrier density. We therefore conclude that charge transfer between MoS_2 and QDs is either absent or does not depend on gate voltage. The lack of

PL modulation in QD/graphene devices further highlights the advantage of 2DSCs for modulation of QDs in the visible (as opposed to IR[94,95]) range. Furthermore, we see that QD/2DSC hybrids can be used for selective modulation of QDs emitting at different wavelengths.

3.5. Conclusions

In summary, we demonstrated electrical control of the near-field energy transfer between QDs and two-dimensional semiconductors (MoS_2, WS_2). We found that it is related to modulation of excitonic absorption of 2D semiconductors, and achieved ~75% modulation of QD photoluminescence in the visible range. It is instructive to compare our approach to other existing schemes to control photoluminescence of QDs via electrical signals. Some of the existing schemes utilize electrochemical injection of charge carriers into QDs,[112,113] electron-hole dissociation under applied electric fields,[120] or controlled Stark shifts.[121] In all of these schemes, electrical fields are applied directly to the QDs. In our approach the electric field changes the parameters of a two-dimensional semiconductor and is absent at the location of QDs. We do not expect electrochemical modification of QDs. The operating principle of our scheme – electrical control over the QD/2DSC FRET rate – can be extended to other nanoemitters. Finally, QDs emitting at different wavelengths over the visible and IR ranges can be modulated by choosing two-dimensional semiconductors with varied bandgaps (e.g.: WSe_2, WS_2, $MoSe_2$).

We envision several potential improvements in our system. FRET efficiency, and hence the efficiency of PL modulation, can be increased by reducing the distance between QDs and 2DSCs (equations (3.1) and (3.3)). This can be achieved by either reducing QD shell-size or by shortening QD ligands. Additionally, 2DSCs could be gated more efficiently using ultrathin gate dielectrics. The advances in CVD growth[122,123] of 2DSCs could lead to inexpensive fabrication

of large-scale QD/2DSC hybrids. Overall, QD/2DSCs hybrids could be used as efficient and electrically tunable light sources operating anywhere in the visible to IR spectral range. Potential applications for such devices range from solid-state lighting and high-resolution passive ("e-ink") displays to biosensors.

3.6. Methods

Synthesis of CdS_xSe_{1-x} Graded Alloy Quantum Dots. This one-pot synthetic procedure is based on a method published recently by Harrison *et al*.[101] First, 1 mmol CdO (0.128 g), 1.3 mL oleic acid (HOA), and 20 mL 1-octadecene (ODE) were heated to 100°C under vacuum for 10 minutes, and subsequently purged with Ar. The temperature was increased to 260°C and the conversion of red CdO to colorless Cd-oleate was monitored to completion, after which the reaction temperature was reduced to 220°C. Solutions of S:Tributyl phosphate (0.75 M) and Se:Tributyl phosphate (0.75 M) in ODE were prepared separately and 0.8 mL aliquots of each were pulled into the same syringe. The S/Se aliquot was swiftly injected into the Cd-oleate flask at 220°C and the reaction was allowed to proceed for 2hrs. The nanocrystals were cooled and precipitated with a 3:1 mixture of butanol and ethanol, resuspended in toluene, and precipitated twice more with pure ethanol. After being finally suspended in toluene, the nanocrystals were passed through a 0.45μm filter and stored.

QD/MoS_2 device fabrication. Cr/Au (2nm/30nm) electrodes were deposited on SiO_2 substrates. The substrates were then cleaned in a piranha solution (1:3 H_2O_2:H_2SO_4) for 1 hour, made hydrophilic through O_2 plasma treatment (30s), and functionalized in 1mM solution of (3-Mercaptopropyl) trimethoxysilane in hexane for 10 min. Functionalized substrates were washed in a hexane bath for 1 min, rinsed in isopropanol, and blow-dried. To assemble a uniform film of QDs, functionalized substrates were placed into 5mg/ml solution of CdSSe for 30mins and rinsed

gently afterwards with toluene. To transfer MoS_2 onto QDs, we followed the recipe developed by Zomer et al.[108] We spun Elvacite polymer (~1μm thick) onto PDMS/clear Scotch tape sandwich structure. The structure was baked at 90°C for 5mins. Monolayer MoS_2 was exfoliated onto Elvacite and verified using optical microscopy and Raman spectroscopy. MoS_2 was aligned with Au electrodes, brought into contact with QD films and baked at 120°C. The PDMS/polymer layer was then mechanically separated from the MoS_2/QD stack. To remove the polymer residues, the MoS_2/QD stack was soaked in acetone for 15 min. Finally, we created the solid electrolyte gate by placing a drop of $CsClO_4$ salt in poly(ethylene) oxide (PEO) matrix dissolved in acetonitrile and drying it for 2hrs at room temperature. A second gate electrode close to MoS_2 was used to contact the solid electrolyte.

PL measurements. PL spectra were recorded at ambient conditions using a Thermo Scientific DXR Raman microscope with a 100μW, 532nm (~2.3eV) laser as an excitation source. MoS_2 was electrically gated using a Keithley 2400 sourcemeter connected to the solid electrolyte. PL modulation of MoS_2 was used to confirm gating efficiency. PL images were collected using a conventional fluorescence microscopy setup with a 605-615nm bandpass filter and green light (530–590 nm) excitation.

Time resolved PL measurements. PL lifetimes of QDs were recorded using a modified version of a home-built confocal microscope described previously.[124] A 400 nm pulsed beam with a repetition rate of 250kHz was reflected from a 410nm long-pass dichroic filter (Omega Optics 3RD410LP) and focused through a water immersion objective to a confocal spot on the QD layer of the fabricated devices. PL was collected through the objective and subsequently passed through the dichroic filter and a 610 ± 5nm bandpass filter to select for QD PL. The QD photoluminescence was then focused onto the array of a single photon avalanche diode (Micro

Photon Devices PDM series SPAD). Lifetime data was collected in the form of single photon events *via* a time correlated single photon counting (TCSPC) correlator (PicoHarp 300) with a time resolution of 4ps. Time-resolved PL from MoS_2 was measured using a grating spectrometer (Acton) coupled to a streak camera system (Hamamatsu). The second harmonic of a femtosecond Ti:sapphire laser with 450 nm pump pulses, 100fs in duration was used for excitation. Two-dimensional spectrograms were acquired in photon-counting mode with 2nm spectral resolution and a minimum 3ps temporal resolution. Time-resolved PL spectra were fitted by a tri-exponential function and lifetimes were estimated as weighted averages of three decay rates.

Absorption/transmittance modulation measurements. Standard differential reflectivity measurements could not be performed on our samples due to the non-uniformity of the solid electrolyte layer. Instead, we used confocal transmission microscopy to determine absorbance/transmittance of gated MoS_2 devices on transparent glass substrates. A broad (~1mm) light beam from a fiber-coupled halogen light source was used to illuminate our sample. Light passed through the sample was collected through a 40X objective and was further magnified ~10 times and focused on a screen with a ~0.5mm diameter pinhole. The pinhole blocks the light from the rest of the sample while transmitting light that passes through MoS_2. The spectrum of the transmitted light as a function of gate voltage was recorded using Shamrock 303i spectrometer. We note that due to the low quantum yield of MoS_2,[89] its PL cannot interfere with our absorption measurements. Differential transmittance measurements of MoS_2 devices on glass without the solid electrolyte layer (Fig. 3.1b) were obtained using the same technique.

CHAPTER 4. DYNAMIC SCREENING OF 2D EXCITONIC COMPLEXES

4.1. Introduction

In this section we will study perhaps the most complex type of interactions between excitonic complexes and their environment – dynamic screening. In chapter 3 we discussed unidirectional energy transfer from environment to an exciton. However, in the case of screening, a reverse process also should be considered: the exciton perturbs and polarizes the environment and the environment, in turn, exerts electric potential on the exciton. Thus, screening can be considered a two-way, or in other words, mutual interaction between an exciton and its environment.

In the most general case, excitonic complexes (EC) including excitons, trions, and biexcitons can be viewed as solid state analogs of atoms and molecules. Many fundamental atomic physics phenomena such as Bose-Einstein condensation, the Lamb shift, and the fine structure are also observed in ECs[125-127]. One of the key differences between ECs and atomic systems is the size – nanometers for ECs and Angstroms for atoms. While electric fields inside atoms are not perturbed by the environment, the fields in much larger ECs propagate into the surrounding medium and are screened by it. The dielectric properties of the environment can often be adequately described by a *dielectric constant* ε . In that case, the EC binding energy E_{bind} can be determined by solving the Schrodinger equation with screened interaction potential V calculated from the Poisson equation. Many realistic dielectrics, however, are characterized by *dielectric function* $\varepsilon(\omega)$ with pronounced frequency-dependence. In that much more complex but experimentally relevant case[1,2,128], screening becomes *dynamic*, i.e. frequency-dependent. The following question arises naturally: how does one calculate the EC binding energies for frequency-dependent environments?

Dynamic screening effects are especially interesting in two-dimensional semiconductors from the group of transition metal dichalcogenides (TMDCs). As mentioned in chapter 1, these materials feature a gamut of tightly-bound ECs with binding energies as large as 0.7eV[10,16]. The screening of the ECs, either by their microenvironment[1,129] or by free carriers[9], is especially strong due to the atomic thickness of TMDCs (Fig. 1a). So far, screening in TMDCs has been modeled as static with the dielectric constant taken either at zero[1,2] or optical[2-4] frequencies. While this approach is justified for some systems, for others it may lead to large errors. Although there have been no attempts – to the best of our knowledge – to examine dynamic screening of ECs in TMDCs, theoretical approaches have been developed for conventional semiconductors[130-133]. Unfortunately, these approaches rely on precise knowledge of properties of specific materials and/or require numerical solution of the Bethe-Salpeter equation, and hence are impractical for many realistic systems.

In this chapter, we develop an analytical model providing intuitive understanding of the screening process. We show that even in the case of dynamic screening, EC binding energies can still be calculated using dielectric functions and screened interaction potentials taken at a certain effective frequency that depends on EC symmetries. We experimentally test the model by studying ECs in monolayer TMDCs coupled to metallic, semiconducting, and liquid environments with frequency-dependent dielectric functions.

4.2. Setting up the problem

The EC is a system of electrons (e) and holes (h) bound by an electric field, e.g. neutral exciton (e+h), charged exciton also known as trion (2e+h or e+2h), defect-bound exciton (modeled as a trion with one particle being static), etc. We start with a simple semiclassical model of an exciton: two oppositely charged particles revolving around each other inside a homogeneous

electrically polarizable medium. In a symmetric case of equally massive particles, $m_e=m_h$, an electron and a hole revolve around their common center of mass with a frequency ω_{rot}. The combined electric field of the particles and hence the polarization of the medium oscillate at the same frequency ω_{rot}. In the opposite asymmetric case, $m_h>>m_e$, the hole is static while the electron revolves around it. Correspondingly, the total electric field created by the charges will have both static and time-dependent components (see Supplementary Information S1). Thus, frequencies relevant for screening of interparticle interactions should depend on EC symmetries in addition to the characteristic frequency ω_{rot} and related binding energy $E_{bind} \sim \hbar\omega_{rot}$.

We now approach the problem of dynamic screening analytically. Let EC eigenvectors $|S\rangle$ and eigenenergies E_S be the solutions of the Schrodinger equation with a frequency-independent interparticle interaction potential. The screening becomes dynamic due to medium excitations j_{med} such as plasmons or phonons. The corresponding correction to the EC ground state energy can be obtained using the second-order perturbation theory:

$$\Delta E_0 = -\sum_{S,j} \frac{\left|\langle S|\langle j_{med}|H_{\text{int}}|0_{med}\rangle|0\rangle\right|^2}{E_{S0}+E_{j0}}. \qquad (4.1)$$

Here, the perturbation H_{int} describes coulombic interactions of the EC with the medium and the summation is over all possible states of the EC and of the environment. Later we show that while exact expressions for $|j_{med}\rangle$ and H_{int} depend on the structure of a particular solid state system and can be quite complex, knowing their explicit form is not necessary for calculating (4.1). The multi-index $S=\{n,q\}$ consists of an index n describing internal excitations of the EC (Rydberg series) and the total momentum q of the EC as a whole. Finally, E_{S0} and E_{j0} are the transition energies

between ground and excited states of the EC and the medium respectively. Evidently, ΔE_0 depends on EC transition energies E_{S0} starting with $E_{00}=0$.

Instead of burdensome expressions for $|j_{med}\rangle$ and H_{int}, experimentally accessible dielectric function can be used to describe medium dielectric response. Then, the Poisson equation with medium dielectric constants evaluated at each frequency ω yields the dynamically screened ω-dependent interaction potential, $V(\omega)$. We note that $V(\omega)$ may have a complex spatial or, equivalently, momentum(q)-dependence. For example, for an EC in a two-dimensional material sandwiched between two dielectrics it is evaluated using the Keldysh potential[15]. We, however, do not write this q-dependence explicitly, since our main focus is the frequency-dependence of interactions. The interaction potential $V(\omega)$ consists of unperturbed frequency-independent potential[1] V_0 and complex-valued dynamic term $V_s(\omega)=V_s'(\omega)+iV_s''(\omega)$, henceforth referred to as the *screening potential*. Treating $V_s(\omega)$ as a perturbation potential, we can rewrite equation (4.1) without explicit involvement of j_{med} [130,131]:

$$\Delta E_0 = -\frac{1}{2}\frac{1}{A}\sum_S |\rho_{S0}|^2 \tilde{V}_s(E_{S0}/\hbar). \tag{4.2}$$

Here A is the crystal volume, $\tilde{V}_s(E_{S0})=2\pi^{-1}\int_0^\infty V_s''(\omega)(\omega+E_{S0}/\hbar)^{-1}d\omega$ [130], and $\rho_{S0}=\langle S|\rho(q)|0\rangle$ is a charge density operator in momentum space "sandwiched" between EC ground and excited state-vectors (See Supplementary Information S1). By analogy with transition

[1] calculated at a frequency where dielectric function is approximately constant.

dipole moment, ρ_{S0} can be also called transition charge density. Throughout the paper we use unitless elementary charge e =1.

4.3. Relevant screening frequencies

While it is possible to numerically compute ΔE_0 from equation (4.2), such calculations require evaluation of wavefunctions for all of the EC excited states. This is complex even for neutral excitons and impractical for larger ECs. However, we can further simplify equation (4.2) by using the general properties of $\tilde{V}_s$ and ρ_{S0} (see Supplementary Information S1):

(a) Frequency-integral $\tilde{V}_s$ can be expressed, using the Kramers-Kronig relations, as frequency-smoothened real part of the screening potential V_s':

$$\tilde{V}_s\left(E_{S0}\right) = \int_{-\infty}^{\infty} f\left(\ln E_{S0}/\hbar - \ln\omega\right) V_s'\left(\omega\right) d\ln\omega\,, \tag{4.3}$$

where $f(x) = 2\pi^{-2}x/\sinh x$ is a normalized bell-shaped distribution function with a vanishing mean value and standard deviation of ~2. According to (4.3), $\tilde{V}_s(E_{S0})$ can simply be approximated by a real part of the screening potential $\tilde{V}_s(E_{S0}) \cong V_s'(E_{S0}/\hbar)$, provided that $V_s'\left(\omega\right)$ is a slow-varying function of frequency. This approximation is valid for many real media[134-137] and is used henceforth to simplify derivations.

(b) Transition charge density created by an electron and a hole – as can be shown analytically – vanishes if $|0\rangle$ and $|S\rangle$ are both symmetric with respect to exchange between electron and hole coordinates $r_e \leftrightarrow r_h$. In the case of such *symmetric transition*, the contributions to ρ_{S0} from an electron and a hole are equal in magnitude and opposite in sign and therefore cancel

each other out. Thus, only the *asymmetric* transitions contribute to the sum in (4.2). This condition is analogous to selection rules in atomic physics. As a result, the minimal value $E_{\min}$ of the transition energy E_{S0}, contributing to the sum in (4.2) is the *energy difference* between *the ground state* and *the lowest asymmetric state*. The summation in equations (1,2) also has a characteristic upper-bound cutoff energy of the order of EC binding energy $E_{\max} \sim |E_{bind}|$ [138,139]: due to decreasing overlap between $|0\rangle$ and $|S\rangle$, the terms corresponding to transition energies above that cutoff quickly decay with increasing E_{S0}, allowing the sum in (4.2) to converge. Thus, only some of the lower-energy terms in (4.2) effectively contribute to ΔE_0.

(c) The summation in equation (4.2) can be further simplified by replacing the frequency-dependent function $V_s'(E_{S0}/\hbar)$ by a frequency-independent mean value $V_s'(E_{eff}/\hbar)$ where effective energy E_{eff} is a constant lying between lower and upper energy bounds, $E_{\min} < E_{eff} < E_{\max}$. This assumption of static screening allows one to treat the EC as a set of particles interacting via frequency-independent potential $V_0 + V_s'(E_{eff}/\hbar) = \mathrm{Re}V(E_{eff}/\hbar)$. In this case, the perturbed ground state energy is

$$E_0 + \Delta E_0 = \langle 0|T + \frac{1}{2}\sum_{j,k} Q_j Q_k \left(V_0(r_{jk}) + V_s'(r_{jk}, E_{eff}/\hbar)\right)|0\rangle, \qquad (4.4)$$

where Q_j is the charge of the *j*-th particle, r_{jk} - interparticle distance and T - is the total kinetic energy of all the particles in the EC.

It is instructive to consider examples clarifying the evaluation of the lower-bound energy $E_{\min}$. In the case of a neutral exciton with equal electron and hole masses[11], the ground state *n=0*

state is symmetric[2]. Then, the energy of the first *asymmetric* transition is $E_{\min} \approx E_{1,0} = E_{n=1} - E_{n=0}$, which typically is of the same order as $|E_{bind}|$ [2]. Other common ECs such as trions, defect-bound excitons or neutral excitons with uneven *e*- and *h*-masses behave differently. Their ground state wavefunctions are inherently asymmetric with respect to $r_e \leftrightarrow r_h$ exchange[16]. The lowest asymmetric transition for such ECs is purely translational (with no change in n) with $E_{\min} \to 0$. Realistically, an EC may decay before the medium has enough time to get fully polarized. Hence, the effective $E_{\min}$ is not exactly zero, but is limited by the inverse characteristic lifetime $\sim \tau^{-1}$ of the particles constituting the EC.

Equations (4.3, 4.4) along with the estimates of the effective energy E_{eff} constitute our main theoretical result. In (4.4), we effectively replace the dynamically screening medium by a medium with a static dielectric constant $\varepsilon(E_{eff}/\hbar)$. To enable experimental predictions from (4.4), we note that the 'diagonal' terms with $k = j$ represent *self-interaction* of each carrier with its image charges. 'Off-diagonal' terms with $k \neq j$ account for screening of *interparticle interactions* (i.e. EC binding). Within simple, but widely used effective-medium approximations for interaction potentials, calculation of self-energies is very susceptible to small uncertainties in microscopic structure of the investigated system and can even yield divergent results[139]. However, the binding energy, calculated using off-diagonal ($k \neq j$) terms in (4.4), can still serve as a proxy for

[2] For a realistic system of *nearly* equal *e*- and *h*- masses in TMDC, then ρ_{00} is proportional to mass discrepancy between electron and hole (2~20%). Hence, $|\rho_{00}|^2$, entering (4.2) does not exceed ~4% compared to the case of vastly different masses.

evaluating strength of interparticle interactions, screened by the medium with effective dielectric constant $\varepsilon(E_{eff}/\hbar)$.

In summary: the range of binding energies of ECs *dynamically* screened by environment with dielectric function $\varepsilon(\omega)$ can be evaluated, to the second order of the perturbation theory, by simply solving the EC Schrodinger equation with the *effective dielectric constants*, obtained from the true frequency-dependent dielectric function evaluated at two limiting frequencies: $\omega_{\min} = E_{\min}/\hbar$ and $\omega_{\max} = E_{\max}/\hbar \sim |E_{bind}|/\hbar$. Binding energies obtained from these two cases are the upper and the lower bounds for the actual binding energy of the EC. The lower bound depends on the EC symmetry: $E_{\min} \approx E_{1,0} \sim |E_{bind}|$ for symmetric charge-neutral ECs with equal *e/h* masses and $E_{\min} \sim \hbar/\tau$ (inverse lifetime of particles constituting the EC) for asymmetric ECs with unequal *e*/*h*-masses or non-zero net charge. In some specific cases the problem can be simplified further. For example, in the case of a long-lived exciton with $m_h >> m_e$, a heavy hole can be effectively treated as static and its field – as constant. Such a field, and hence, exciton binding will be screened by the medium only at zero effective frequency $\omega = 0$ yielding static effective dielectric constant $\varepsilon(\omega = 0)$. Below we will demonstrate that for many realistic cases, ε does not change significantly between frequencies $E_{\min}/\hbar$ and $E_{\max}/\hbar$, which allows us to make experimentally testable predictions regarding screening of EC binding.

4.4. Setting up the experiment

In order to test the developed theory, we measure the effect of different dispersive environments on binding energies of different types of ECs in a monolayer TMDC. We choose monolayer WS_2 as a test bed since this material has a variety of tightly bound ECs[2,8-10,140,141]

that produce narrow and well-resolved peaks in photoluminescence (PL) spectra[2,7-10]. We focus on three prominent excitonic species (Fig.1a):

(a) neutral exciton (X^0). It has nearly identical electron and hole masses[11,16] and is symmetric according to our classification. Therefore, interparticle interactions are expected to be screened at effective energy in the mid-IR range: between the first excited state transition energy of ~130meV[2] and binding energy of ~320meV[2].

(b) trion (X^-). This charged state is classified as asymmetric. We expect trion screening in the THz range: between ~0.5meV, which corresponds to ~10ps lifetime[142,143], and the binding energy ~30meV[10].

(c) defect-bound exciton[140,141] (X^D), treated here as a neutral exciton bound to a static charged impurity[3]. The binding energy of X^D is ~150meV, which agrees with our numerical model described below. Note that the binding energies of X^D and X^- are defined with respect to the energy of a neutral exciton. The electric field of a static charged impurity, binding the exciton, is screened at zero frequency. This situation is similar to the example of a long-lived strongly asymmetric exciton considered above[4]. Therefore, defect-bound excitons are expected to be screened at zero frequency.

To test the dynamic screening of these ECs, we choose the media with qualitatively different dielectric functions in the range of relevant frequencies (Fig.1b):

[3] At this point the origin of impurities is not completely clear. However, large binding energy of X^D and its agreement with our numerical modelling (electron+hole+static charge) suggests that defect-related excitons can be treated as a neutral excitons bound to deep charged defects.

[4] For defect-bound exciton it is energetically favorable to have an electron highly localized near an impurity (if impurity charge is positive) and hole – delocalized. Such a distribution of density function makes the defect-bound exciton indeed similar to a highly asymmetric neutral exciton.

(i) metallic medium. Two-dimensional semimetal graphene exemplifies a metallic-type dielectric response $\varepsilon \sim \omega^{-2}$. Specifically, $\varepsilon(\omega)$ for graphene is large (>10) for ω from 0 to THz and is close to 1 in the IR range.

(ii) liquid medium. We use ionic liquid DMA-TFSI[5], for which $\varepsilon(\omega)$ is large (>10) at sub-GHz frequencies and is insignificant above 1THz.

(iii) semiconducting medium. For semiconductors, $\varepsilon(\omega)$ is roughly constant in a broad range of frequencies. In our experiments, a monolayer MoS_2 transferred onto our device serves as a semiconducting screening layer with $\varepsilon(\omega)$~15 in IR-to-visible range and ~5 in the sub-THz range.

Figure 1b shows the dielectric functions for each medium along with frequency ranges (shown as vertical bands) relevant for screening of X^0, X^-, and X^D. The dielectric functions are relatively constant within each band. Summarizing, we expect the binding energy of neutral excitons to be strongly affected by semiconducting but not liquid or metallic environment. For trions, we expect strong screening by metallic environment only. Finally, defect-bound excitons should be affected by metallic and liquid environments. We cannot make a definitive qualitative prediction of the effect of the semiconducting medium on X^- and X^D because, in relevant sub-THz range, MoS_2 dielectric constant (ε~5) cannot be considered neither large (>10) nor small (~1).

4.5. Measurements

Measurements were performed on monolayer WS_2 flakes, exfoliated on Si/SiO_2 substrates with patterned gold electrodes. Electrostatic gating was used to control the Fermi level and isolate the contribution of free-carrier screening[9,10].

[5] diethyl methyl(2-methoxyethyl)ammonium bis(trifluoromethylsulfonyl)imide

In order to study X^D we induced defects using argon plasma[141]. We begin our measurements by recording PL spectra (532nm, ~20μW laser excitation focused into a ~2μm spot) at T=78K for pristine WS_2 devices without any material on top (Fig.4.1c, WS_2 device).

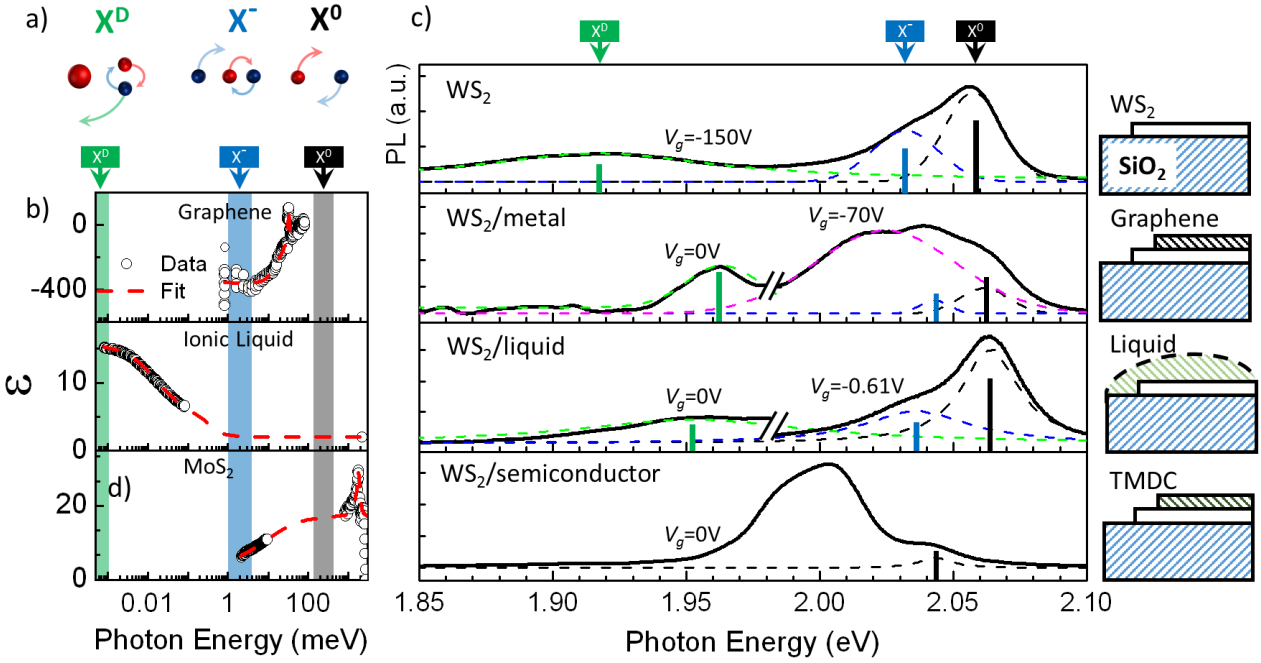

Figure 4.1. Effect of environments on WS_2 PL spectra. (a) top: schematic illustrations of X^D (static impurity is in the middle), X^- and X^0. **(b)** Dielectric functions of the screening materials: graphene[134], ionic liquid[135,136], and monolayer MoS_2[137]. Since experimental dielectric functions are not available for the entire frequency range, we interpolate them using double Lorentzian fitting. **(c)** PL spectra of WS_2 in different environments – schematics are on the right. Dashed curves are fitted excitonic peaks. The symbol "//" separates curves obtained from different samples/at different gate voltages. Voltage is shown above each curve. As in-situ gating with ionic liquid is impossible at low temperatures, the data for the WS_2/liquid device (right curve) were obtained at 240K and artificially blue-shifted by 40meV to account for thermal shift of the peaks[8].

The well-known peaks in the PL spectra at ~2.06eV (black dashed line), ~2.03eV (blue dashed line), ~1.92eV (green dashed line) are identified as stemming from neutral excitons X^0, trions X^- and defect-bound excitons X^D respectively [8-10,16,141]. The peak at ~2.02eV observed in some

devices (e.g. Fig.4.1c, pink dashed line) is likely associated with an additional trion state[9,126,144] and is not analyzed further.

We modify the dielectric environment of the WS_2 flake by either mechanically transferring[145] monolayer graphene or MoS_2 (WS_2/metal and WS_2/semiconductor device respectively), or dropcasting a layer ionic liquid (WS_2/liquid device). We then re-acquire the PL spectra. We observe large and reproducible shifts of all three excitonic peaks (Fig.4.1c). Note that environmental factors other than screening (i.e., induced doping, strain and chemical modifications) may also cause peak shifts[9,10,146,147]. However, as shown below and in the Supplementary Information S3, the observed shifts are too strong to be explained by changes in the doping level. The effects of strain are shown to be weak by comparing PL spectra of transferred heterostructures and naturally grown WS_2 bilayers. We also see no evidence of chemical modifications in WS_2/liquid devices as observed shifts are reversed by *removing* the ionic liquid. Thus, we interpret observed shifts as originating from the dielectric screening of excitons. To compare these shifts with theory, we extract exciton binding energies for different types of environment. The binding energies of trions and defect-bound excitons are determined as $|E_{bind}(\mathrm{X}^{-,D})| = Pos(\mathrm{X}^{-,D}) - Pos(\mathrm{X}^0)$, where $Pos(\mathrm{X})$ is the energy position of a particular excitonic peak in PL spectrum. In pristine devices, we observe $|E_{bind}(\mathrm{X}^-)|$ ~25meV and $|E_{bind}(\mathrm{X}^D)|$~140meV, close to literature values[9,10,141]. Unfortunately, $|E_{bind}(\mathrm{X}^0)|$ cannot be measured directly using absorption or PL spectroscopies as these techniques are unable to directly probe the single-particle electronic bandgap [2,10,148]. We rely on the on the experiments by Chernikov, et *al*.[2,9] measuring $|E_{bind}(\mathrm{X}^0)|$~320meV for uncovered $Si/SiO_2/WS_2$ devices similar to ours, and showing 1meV red-shift in $Pos(\mathrm{X}^0)$ per ~6meV decrease in the exciton binding

energy (studied by controlling the binding energy by either varying the number of layers or the carrier density in WS_2). These observations allow us to convert the screening-induced shifts of the X^0 PL peak position into its effective binding energy.

Figure 2 summarizing the effects of metallic, semiconducting, and liquid environments on the binding energies of X^0, X^-, and X^D (square symbols) constitutes our main experimental result. The following trends are evident: The extracted binding energy of X^0 decreases by 120±40meV (~40%) in the WS_2/semiconductor sample. This conforms well with studies performed on bi- and multi-layer TMDCs[2,13,149]. For X^-, the binding energy is downshifted by 10±3meV (~30%) due to the presence of graphene. The binding energy of X^D is reduced by 40±20meV (~30%) in presence of both metallic and liquid environments. In all other measured cases EC peak shifts are insignificant within our error bars. These trends agree well with our qualitative predictions. In case of WS_2/metal and WS_2/semiconductor samples we could not bring WS_2 close to depletion, likely due to strong effects of charge transfer in these heterostructures[29]. Nevertheless, observed shifts exceed possible doping-induced effects: trion binding energy in presence of graphene becomes as low as 19meV, and neutral exciton red-shifts to 2.045eV in semiconductor-capped devices. These values are significantly below the energies achieved by doping alone[9,10](see Supplementary Information S3).

4.6. Quantitative comparison with theory

To further verify our model, we perform quantitative estimates of ECs binding energies (see Supplementary Information S2). We computationally solve the Schrodinger equation for 2- or 3-body systems using variational approach[150-152] with *e*- and *h*-masses of $0.45m_0$[11,12] and infinite mass for the defect charge. Interparticle interactions are modelled by the Keldysh potential[15] calculated using WS_2 and medium dielectric functions taken at effective frequency

ω. Upper- and lower-bound estimates for EC binding energies ($E_{bind}(\omega_{\min})$ and $E_{bind}(\omega_{\max})$) are obtained by setting ω to $\omega_{\min} = E_{\min}/\hbar$ and $\omega_{\max} = |E_{bind}|/\hbar$ as prescribed by our theoretical model.

The ranges of theoretical EC binding energies – from $E_{bind}(\omega_{\min})$ to $E_{bind}(\omega_{\max})$ – are shown as shaded ovals in Fig.4.2. Observed values of X^0 and X^- binding energies are within the theoretically expected range for all media. Shifts of X^D, calculated assuming only zero-frequency screening, exceed experimental ones, probably due finite spatial separation between measured EC and the medium, which is assumed to be negligible in our model. In the case of X^- and X^D in presence of a semiconductor environment, predicted shifts are too subtle to be experimentally tested with certainty and were not measured as that would require higher accuracy of computational models and measurement techniques. Overall, we believe that this quantitative agreement is remarkable for a minimal model with no free parameters.

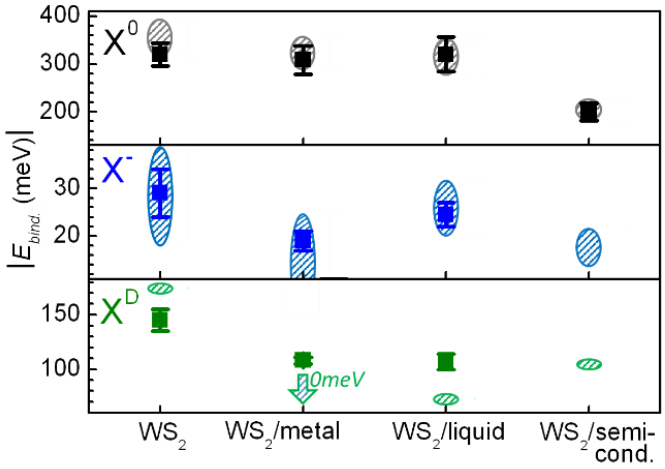

Figure 4.2. Summary of experimental and theoretical results. Square symbols are experimentally observed EC binding energies in presence of different screening materials, while ovals show the range of theoretically predicted values. For both X^- and X^D in WS_2/metal devices the calculated energy range starts at zero (shown by downward arrow).

4.7. Conclusions

The theory of excitonic complexes in dynamically-screening media was developed and confirmed experimentally. We obtained the binding energies of dynamically screened ECs by solving the Schrodinger equation with *effectively static* interaction potentials calculated at the *fixed effective* frequency. This frequency depends on the symmetries of the wavefunctions and the binding energies of ECs. The model was tested and confirmed experimentally by using neutral, charged, and defect-bound excitons in two-dimensional semiconductor WS_2 screened by metallic, semiconducting and liquid environments. The developed approach is general and can be applied to diverse systems of quasiparticles, interacting via electric fields – including plasmons, excitonic molecules, and polaritons – screened by various media.

Our simple dynamic screening model may help to re-interpret and clarify a wide range of previous experiments were static screening was assumed. For example, the assumption of zero-frequency screening of two-dimensional ECs by liquids ($\varepsilon(\omega = 0) \sim 50$) has led to the appearance of outlying data points, overestimation of exciton binding energies[1,153] and underestimation of effective electron mass by two orders of magnitude[21]. Moderate shifts in exciton energies observed in these experiments are more consistent with screening at optical frequencies, as predicted by our model, where most liquids have $\varepsilon \sim 2$. Another important example is the inconsistency in the reported neutral exciton binding energy in monolayer MoS_2, which ranges from 220meV to 660meV depending on the type of measurements and applied models[148,154,155]. The lowest binding energy, 220meV, is obtained by Zhang et *al*.[155] by subtracting the optically measured energy of the excitonic PL peak from the electronic bandgap measured using scanning tunneling spectroscopy. Their measurements were performed using MoS_2 samples on a semimetallic graphite substrate. According to our model, excitonic and free-

particle states are screened by graphite at different effective frequencies, which yields ~400meV difference in corresponding screening-induced energy shifts. This accounts for the discrepancy between the values obtained by Zhang et *al*. and by others[148,154].

Effects of dynamic screening may also have practical applications. For example, it may be possible to probe frequency-dependent dielectric functions of various microscopic environments by measuring relative shifts of different types of ECs (including EC excited states) that are screened at different effective frequencies. This can be interesting for label-free biodetection or chemical sensing.

CHAPTER 5. EXPERIMENTAL SETUP

In order to perform our experiments we designed and used the setup for optoelectric measurements of microscopic objects. It allows us to illuminate microscopic samples with a diffraction-limited light spot and study electrical and optical signals coming from these samples. The sample can be studied inside a cryostat in vacuum and at low temperatures.

The experimental setup for optoelectric measurements consists of five main parts (Fig.5.1):

1. Light source assembly, which combines different sources of light with different powers and wavelengths.
2. Light coupler, which couples the light to a microscope and allows scanning of the beam using a piezoelectric mirror.
3. Microscope, which allows focusing of the beam into a diffraction-limited spot on the sample and imaging of the reflected light.
4. Sample holder: it can be either a cryostat with electrical connections or an ambient-environment sample holder similar to a standard microscope sample holder.
5. Spectrometer, allowing to analyze optical signals.

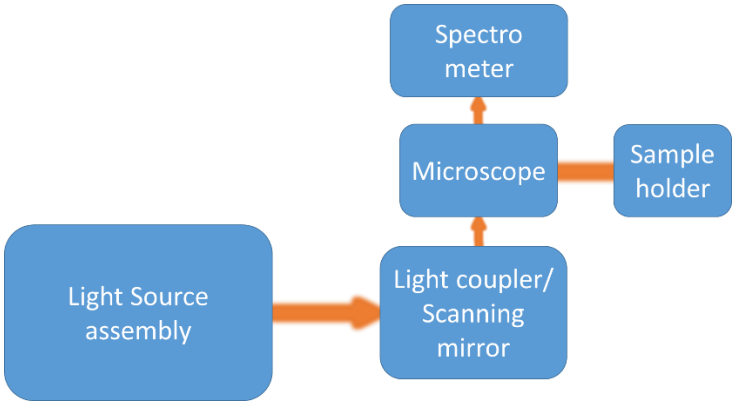

Figure 5.1. General schematics of the setup.

Let us look at these parts and their inner workings in greater detail. It is important to start by introducing a list of notations of optical components:

M – mirror. In figures 5.2–5.7 : reflecting side is shown with the blue color.

FM – flip mirror

STM – semi-transparent mirror which transmits/reflects 50% of the light – essentially a filter with optical density (OD) of ~0.3.

DM – dichroic mirror

SM – scanning mirror on a piezo-electric mount

L – spherical lens. In figures 5.2–5.7: arrows pointing away from each other denote converging lens; otherwise – diverging.

FL – lens on a flip mount

CL – cylindrical lens

A – aperture

LPF – long-pass filter

SPF – short-pass filter

GNDF – gradient neutral density (ND) filter. It is a rectangular ND filter with optical density gradually varying from the left side to the right side of the filter

S – mechanical shutter

5.1. Light source assembly

This part of the setup allows to select a type of a light source that will later be coupled to the microscope. Schematics of the light source assembly is shown in Fig.5.2. It incorporates 4 types of light sources:

Fianium supercontinuum laser. It produces white light with 4W power and the spectral range between 390nm and 2500nm. This source is highly collimated and hence its light can efficiently focused into a diffraction-limited spot for measurements of weakly absorbing materials or for photoluminescence excitation (PLE) measurements needing relatively high, up to 100μW/um^2, power density at the sample.

Tungsten-halogen lamp. This source produces uncollimated white light with 40 – 200W power and 400nm – 1000nm wavelength range. Since this light source has high beam divergence, it cannot be used to for PLE measurements due to low power density of <1μW/um^2 at the sample. The advantage of this light source is its smooth thermal spectrum (Fig.5.2, inset) without sharp peaks, which is convenient for absorption, transmittion and photocurrent measurements. Smooth spectrum allows to minimize errors during normalization of reflectance/transmittance spectra to the incident spectrum. In contrast, some other commonly used light sources such as mercury lamps have prominent spectral peaks. The presence of these peaks may lead to large errors when measured spectra stemming from the sample are normalized to incident ones in vicinity of those spectral peaks.

Violet (405nm) and green (532nm) lasers. These lasers emit collimated light with 20 – 70mW power. This light can be efficiently focused into a diffraction-limited spot for photoluminescence (PL) measurements.

The main purpose of the light source assembly is to make light beams from all these sources collimated and collinear (i.e. going along the same path). Additionally, the light source assembly contains a monochromator allowing us to select the desired wavelength from white light sources such as a halogen lamp or a supercontinuum laser. In combination, this assembly acts as a single highly tunable and universal collimated light source.

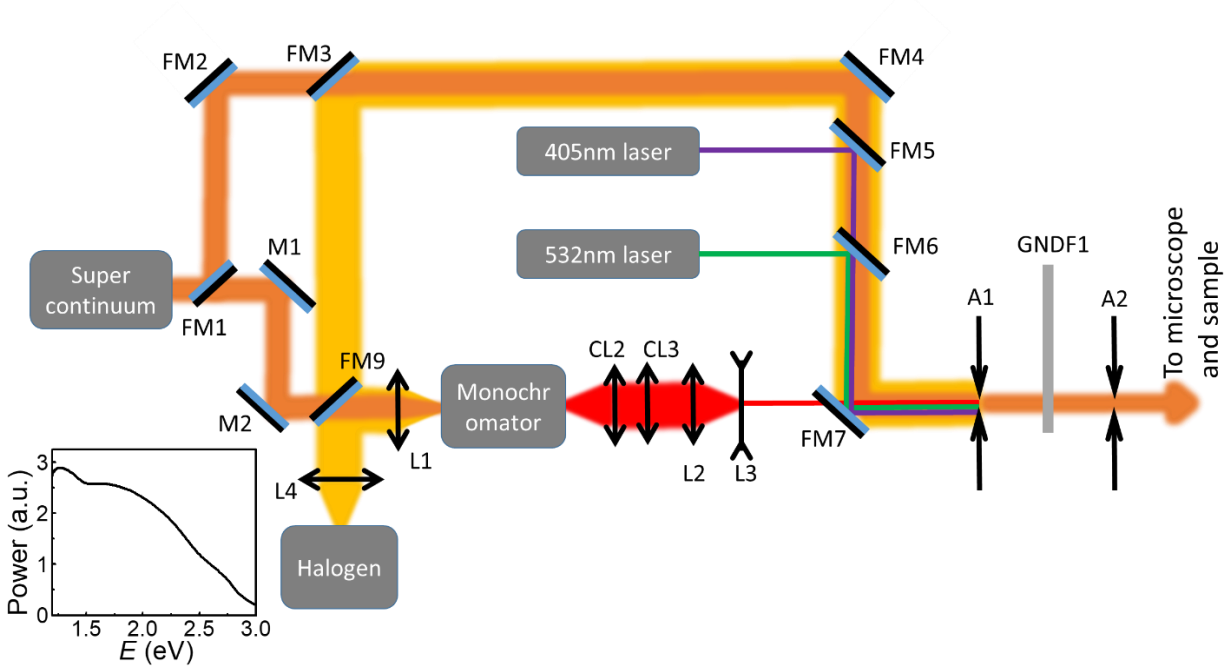

Figure 5.2. Light source assembly. The spectrum of the halogen light source is shown as an inset.

First let us discuss the coupling of white light sources. By controlling flip-mirrors FM1 and FM9, we can choose whether the light from the supercontinuum laser or a halogen lamp enters the monochromator to be used for PLE or photocurrent measurements or if it goes unfiltered around the monochromator to be used for absorption measurements.

By controlling flip-mirrors FM5, FM6 and FM7 we can guide either white light or green/blue laser light to the apertures A1, A2 and consequently to the microscope. Alternatively,

by flipping down and thereby excluding the mirror FM7 we can guide a monochromated light to the microscope.

In order to use a monochromated light for our experiments, the mirror FM1 should be down and FM9 – up. In this configuration the white light either from the supercontinuum laser or from a halogen lamp goes into the monochromator. Lens L1 focuses the white light on a monochromator entrance slit. The desired wavelength range can then then chosen. Lenses L2, L3 are used to collimate the monochromated light and cylindrical lenses CL2, CL3 allow to control its stigmation.

Gradient ND-filter GNDF1, attenuating the light intensity, is placed at the point where the beam has the smallest width. This filter allows us to attenuate power up to 1000 times. By placing additional filters, stronger attenuation can be achieved. Placing the gradient filter at the point where the beam is wider and is comparable to the size of a filter makes the beam less uniform.

Apertures A1 and A2 serve two purposes:

(a) These apertures help focusing non-Gaussian beams at the sample. For example, beams passing through a monochromator or emitted by some solid-state lasers have rectangular cross-sections. Apertures act as pinholes and make these beams more circular. Circular beam can be better focused into a diffraction-limited spot than a rectangular one. However, apertures alone will not make the beam Gaussian and hence will not allow a perfect focusing.

(b) Apertures simplify the alignment process. Mirrors used in the light source assembly have micrometric screws allowing fine tuning of the beam direction. Light path from each light source should be tuned in such a way that the light passes through both apertures. In other words, A1 and A2 determine the final path of the beams stemming from all the light sources. After A1 and A2, all beams are collimated, circular, collinear – with coinciding paths –

and with roughly same diameter. In this case, *all further manipulations with the light will be independent of what light source we choose to use*. After the alignment of the light source assembly has been performed, the user can switch between different light sources by simply flipping the states of the flip-mirrors. Sometimes, however, minor adjustments of the mirror angles may still be needed.

5.2. Light coupler

This part of the setup (Fig.5.3) is used to couple the light generated by the light source assembly to the microscope.

Mirrors M3 and M4 form a periscope that lifts the beam path from the level of the table within 10'' above the optical table surface to a level of a microscope about ~1' above the optical table surface. Mirrors SM1, M5 and lenses L5, L6 allow fine alignment and focusing of the incoming beam to the entrance aperture of the microscope.

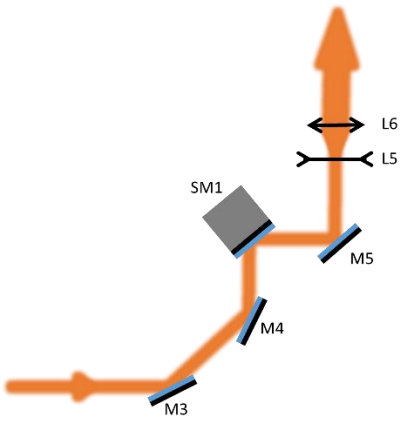

Figure 5.3. Light coupler. Mirrors SM1 and M5 allow fine tuning of the beam path. A Galilean telescope L5+L6 is realized in a cage system and allows to collimate the beam and control its size.

Scanning piezo-electric mirror SM1 allows us to control the beam direction which eventually results in controlling position of the diffraction-limited spot focused on the sample. This mirror can be computer-controlled. This is useful for performing scanning photoluminescence and photocurrent mapping. Together with M5, the mirror SM1 is also used to align the beam to the center of the beam expander formed by lenses L5 and L6. For performing PL measurements, one can also place a short-pass excitation filter SPF1 after L6.

5.3. Microscope

After the beam expander (L5+L6), the collimated light enters a microscope (Fig.5.4).

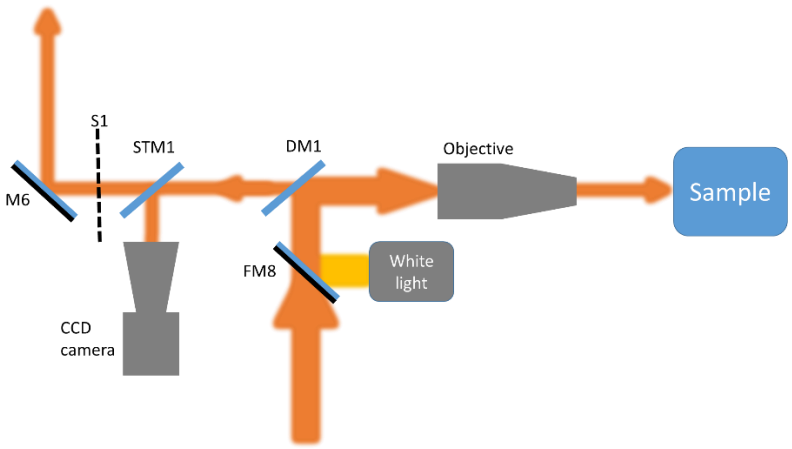

Figure 5.4. Microscope.

A microscope consisting of an objective and a dichroic mirror DM1 has an additional white light source used for imaging. Flip mirror FM8 allows switching between a collimated laser light used for measurements and an uncollimated white light needed for imaging. We use two types of objectives to focus the beam on a sample: 10X objective for rough alignment and 40X objective for precise focusing and measurements. The 40X objective also allows correction of the beam when focusing through a cryostat glass. Semi-transparent mirror STM1 is used to redirect part of

the light to a CCD-camera, which allows us to image the sample and monitor the shape of the laser spot. The light coming out of the microscope can be blocked using a mechanical shutter S1. This is convenient for recording the background signal during absorption and PL-measurements. Finally, the mirror M6 redirects the light further to the spectrometer.

5.4. Spectrometer

After a microscope, light re-emitted by or reflected from the sample is redirected to the spectrometer by the mirror M7 (Fig.5.5). Lens L7 is used to focus the light on the spectrometer entrance slit. It is also possible to place an additional lens FL1 and a screen with a pinhole (FS1) on the way of the beam. Both elements FL1 and FS1 are removable as they are mounted on flip-mounts. By focusing the light onto the pinhole using lens FL1, we can increase the spatial resolution of a system as it is done in standard confocal measurements. This will be discussed in greater details in the "transmittance measurements" section.

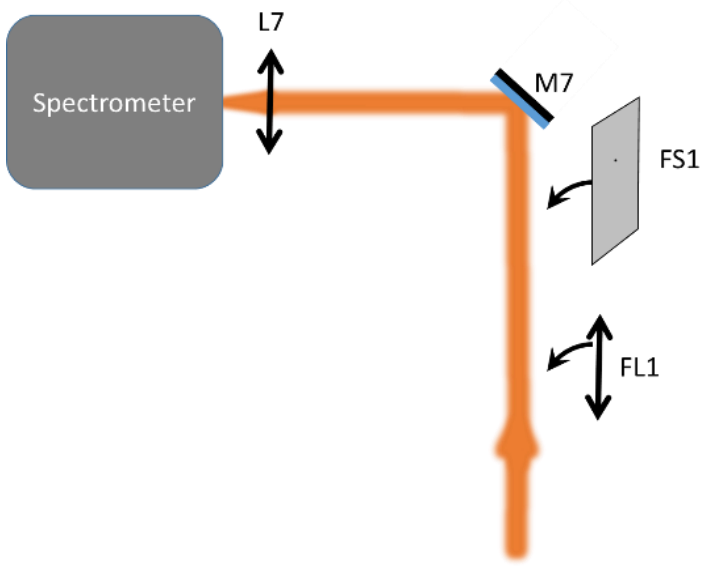

Figure 5.5. Coupling to spectrometer.

5.5. In-situ laser annealing

The optical setup described above can also be used for sample preparation, specifically, for sample cleaning via a procedure that we shall call “laser annealing”. We focus a powerful, up to 10W, beam of mid-IR light generated by a CO_2 laser onto a ~1mm spot on the sample. This allows us to locally heat the sample to temperatures of ~700K. This method does not require heating the entire cryostat and, unlike current annealing[17], can be performed in situ on samples that poorly conduct electricity.

This method is more efficient if performed at low cryostat temperatures: in this case, the debris desorbed from the sample during annealing are re-adsorbed by the cold surfaces around the sample and have lower chance of returning to 2D material surface. Figure 5.6 shows how laser annealing is performed. The laser beam is focused onto the sample into a sub-millimeter spot using ZnSe lens L8 that is transparent in the mid-IR range. The cryostat window should be made of a material transmitting 10.6μm laser light of the CO_2 laser. Barium Fluoride (BaF_2) is an optimal material for such purposes since it transmits light in a wavelength range from 200nm to 20μm. Sine the CO_2 laser light is invisible, we use a collinear red laser beam for alignment of the CO_2 laser beam with the sample. Flip-mirror FM9 is used to switch between annealing and alignment laser beams.

Annealing is performed in short pulses from 1 to 10 sec. After each step the sample is characterized either electrically, via conductivity measurements, or optically via PL or photocurrent spectroscopies. Steps are repeated until the sample obtains desired properties, such as desired Fermi level, peak width, conductivity, photoconductivity, etc.

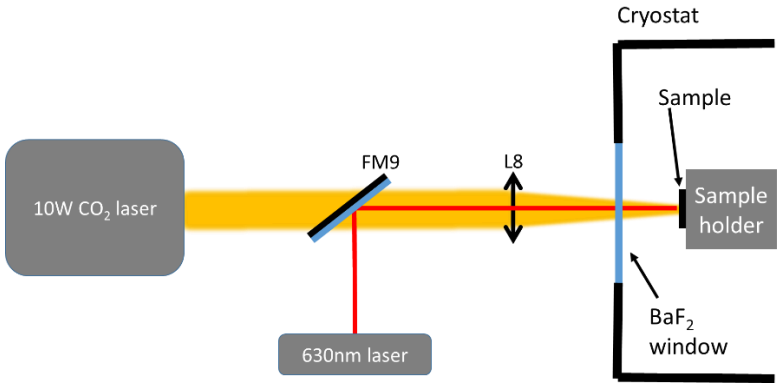

Figure 5.6. Sample annealing schematics.

5.6. Measurements

The primary purpose of the optical setup is performance of various optical and electrooptical measurements. Here we will focus on four types of measurements: photocurrent, photoluminescence, transmittance and reflectance.

Photocurrent spectroscopy.

Basics

Photocurrent measurements are performed by applying voltage between the source and drain electrodes of a 2D device and illuminating the device with the monochromated light of a controlled wavelength. Then, light-induced changes of the device conductivity are recorded as a function of the illumination wavelength. This dependence is called a photocurrent spectrum. Weak photocurrent is measured with the help of a lock-in amplifier.

Light source: requirements, monochromation and calibration.

For better precision of the photocurrent spectroscopy it is recommended to use a light source with a smooth spectral curve. As mentioned above, the spectrum of the incident light should not have peaks and features narrower than the range over which the photocurrent spectrum is

recorded. Since photocurrent signal should be normalized to the intensity of the incident light, division by a function containing sharp peaks causes increased artificial noise in vicinity of those peaks. Therefore, a tungsten-halogen lamp, characterized by a smooth thermal spectrum, is a perfect light source for photocurrent measurements.

In order to vary the wavelength of the incident light, we use a monochromator, which controllably selects a specific wavelength out of the broad spectrum of the white light. The spectrum of the incident light is recorded by placing the calibrated photodetector in the position of the sample. The power on the photodetector is recorded as a function of the central wavelength outputted by the monochromator. The obtained spectrum is then used to normalize the photocurrent spectrum and isolate spectral features of the investigated material from the spectral features of the light source. In order to perform such normalization it is important to make sure that photocurrent stemming from the sample is a linear function of the incident light intensity. Such test should be performed at different wavelengths. Sometimes we notice that the light stemming from some sources, such as halogen lamp, fluctuates with time by ~10%. In this case it is important to measure the photocurrent and the light power simultaneously. In order to do that, the incident beam should be split using semi-transparent mirror and a portion of the incident light should be redirected to the photodetector.

While most photocurrent measurements can be performed with a ~1mm spot size, the beam focused into a diffraction-limited spot can be also used for scanning measurements. Scanning photocurrent spectroscopy allows to measure magnitude and spectrum of photoresponce from different parts of the measured device: source and drain electrical contacts, channel, etc. By deflecting the beam using the piezo scanning mirror SM1, the focused beam can be rastered across the sample in ~10μm range. Exceeding this range is not recommended as it requires strong

deviation of the beam from the optical axis of the beam expander (L5+L6) and microscope objective. This causes loss of power, defocusing and aberrations. The scanning mirror is controlled by applying voltage to its inputs. The voltage, in turn, is computer-controlled using a LabView program and a digital-to-analog converter.

Photoluminescence spectroscopy.

Photoluminescence spectroscopy is perhaps one of the most common types of optical measurements. The sample is illuminated with a focused beam of monochromatic laser light. The light re-emitted by the sample is redirected to the spectrometer. The incident light is passed through a short-pass excitation filter mounted after lens L6. The role of this filter is to prevent long-wavelength "tail" of the incident laser light from interfering with the signal stemming from the sample. The light re-emitted from the sample typically has a longer wavelengths than the excitation light. A long-pass emission filter, placed before shutter S1, transmits the emitted light but prevents the excitation laser beam from entering the spectrometer. For example, for 532nm excitation laser, we typically use a 550nm short-pass excitation filter and a 600nm long-pass emission filter.

Transmittance measurements.

Typically, transmittance measurements require two high-magnification objectives on both sides of the transparent microscopic sample in order to focus the incident light only on a small area of the sample and then collect transmitted light from the same small area. Our setup, however, allows to perform such measurements using only one objective. Figure 5.7 demonstrates the geometry of such measurements. The sample is illuminated from below by the white light that is guided via an optical fiber of large diameter of ~0.5mm. The fiber is mounted on the X-Y micrometric stage to be precisely aligned with the measured sample. The light, passing through the sample is collected by the microscope objective. The lens FL1 controlled by the flip-mount is

placed on the path of the beam in order to focus a sharp image on a white screen FS1 which is also attached to a flip-mount. In a dark room this image is visible to a naked eye. The screen FS1 has a ~1mm pinhole. The position of the sample should be carefully adjusted until the image of the sample is projected on the pinhole. This ensures that only the light passing through the corresponding area of the sample passes through the pinhole and enters the spectrometer. In order to perform transmittance measurements, one needs to record a background spectrum *B*, a reference spectrum *R* – light passing through the substrate near the sample – and spectrum *T* of light passing through the point of the sample. The transmittance signal is then calculated as *(T-B)/(R-B)*.

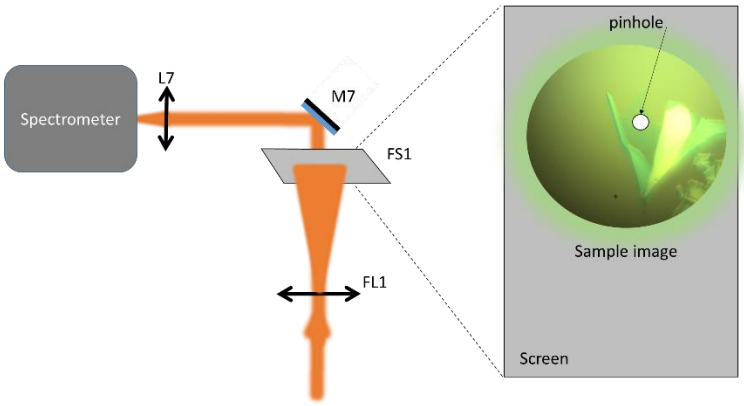

Figure 5.7. Transmittance measurements schematics.

Alignment procedure for the transmittance measurements

First, it is important to make sure that the pinhole is located on the way of the light stemming from the sample. To do that, we need to turn on the pre-aligned laser light with spectrometer entrance slit closed and in absence of the lens FL1 align the pinhole FS1 to the reflected laser light using micrometric screws. Then, after FL1 is put in place, the laser beam should be focused on the pinhole. This procedure ensures that the light passing through the pinhole also penetrates the spectrometer entrance slit. After that the pinhole should not be moved. All

alignment of the sample image with the pinhole is performed by moving the sample and not the pinhole.

Reflectance measurements.

Reflectance measurements can be performed in the following two ways.

1. Similarly to PL measurements: the incident light is focused on a particular spot of the sample, but measurements are performed without the excitation filter. Similarly to transmittance measurements, we need to record a background and reference spectrua and measure differential reflectivity.

2. Similarly to transmittance measurements: the sample is illuminated with the broad (unfocused) white light and spectrum stemming from specific point of the sample is selected by the pinhole on the screen FS1. These types of measurements are identical to transmittance measurements, but in this case the sample is illuminated from the top.

Needless to say, to avoid saturating and potentially damaging the spectrometer, the incident light has to be attenuated by at least 4~5 orders of magnitude.

CHAPTER 6. CONCLUSIONS AND FURTHER RESEARCH

We studied mechanisms of interactions between excitons and their environment. In chapter 2, by means of photocurrent spectroscopy we have shown that in monolayer MoS_2 unaffected by the environment, excitons are tightly bound with the binding energy of $E_{bind.}$>560meV. These excitons can be dissociated by electric fields and create photogenerated charge carriers, yielding photogain of >1000 carriers per photon. Moreover, we observed efficient photogeneration from the C-exciton – exciton stemming from the van-Hove singularity in vicinity of the Γ-point of MoS_2 Brillouin zone. We have theoretically shown that electron and hole constituting such exciton have an unusual Mexican-hat-shaped dispersion relation in the center-of-mass frame.

In chapter 3, we demonstrated that excitons in TMDCs can efficiently interact with their environment via energy transfer. We created samples with a proxy-environment consisting of a 2D array of quantum dots. We proved that quantum dots can efficiently transfer energy to 2D excitons via Forster resonant energy transfer process. This is an example of a simple unidirectional interaction between 2D excitons and their environment. By electrostatically gating our devices and thereby controlling oscillator strength of 2D excitons we have shown that effective strength of exciton-medium interactions can be tuned by more than 500%.

In chapter 4, we demonstrated that 2D excitons can be efficiently screened by their environment. In the case of screening excitons polarize the medium and the polarized medium affects excitons via Coulomb interactions. In the case of environment with frequency-dependent dielectric function, screening becomes dynamic. Then, frequency-dependent interaction potentials cannot be directly plugged into the Schrodinger equation. We developed a general theoretical model that allows to evaluate interactions between excitonic complexes consisting of any number of charged particles, and their frequency-dependent environment. Our model suggests that

interparticle interactions within excitons are screened at a certain effective frequency. This frequency, in turn, depends not only on the exciton binding energy, but also on the symmetries of an exciton wavefunction. Finally, we experimentally confirmed our model, using monolayer WS_2 as a test bed. By surrounding WS_2 with metallic, liquid and semiconducting environments we confirmed that changes in binding energies of neutral, charged and defect-bound excitons agree with our predictions. We demonstrated that in agreement with our model, excitons with different symmetries and binding energies can be screened differently even by the same environment.

As described in chapter 5, we have also designed a universal experimental setup allowing to perform confocal microscopic measurements of nanoscale samples at low temperatures. Our experimental setup allows to image and study various samples via photoluminescence and photoluminescence-excitation spectroscopy, scanning photocurrent spectroscopy, differential reflectivity and transmittance spectroscopies. Finally, we developed a universal technique of in-situ annealing of samples by illuminating them with the focused powerful (<10W) beam of the CO_2 laser.

We applied the obtained results for interpretation of already existing experimental data as well as proposed practical applications of observed effects. For example, controllable energy transfer between 2D materials and other nanoscale emitters can be used for making electrically tunable pixels for displays. Effects of dynamic screening can be applied for probing dielectric functions of various materials at a microscopic scale. Below we propose directions for the future research of topics discussed in chapters 2-4.

6.1. Near-field optical spectroscopy.

Nanoscale emitters described in chapter 3 can be used as light sources for near-field spectroscopy. When such emitters are brought in close proximity to 2D materials it is possible to observe various near-field effects. Conventional far-field photons carry a negligible momentum compared to lattice momenta of electrons. In this section we will show that in contrast to far-field photons, near-field light waves can (i) transfer high momentum to the 2D material and (ii) cause unusual effects such as emergence of a tunable van Hove singularity in graphene.

First, let us consider how a nanoscale emitter of a characteristic size *d* placed on top of a 2D material emits light waves with large wavenumbers and, hence, momenta. Examples of possible nanoscale emitters include quantum dots emitting broad white light spectrum[156], fluorescent dyes, or plasmonic nanostructures. Unlike commonly used far-field light, near-field evanescent electromagnetic waves can be spatially non-uniform on a nanometer scale. Such a non-uniform electric field *E* created by one or several nanoparticles (Fig.6.1b) can be represented as a linear combination of multiple plane waves

$$\vec{E}(\vec{r},t)=\sum_{\vec{k},\omega}\vec{E}_{\vec{k},\omega}\exp\left(i\vec{k}\vec{r}-i\omega t\right). \quad (6.1)$$

Here $\vec{r}$ is the in-plane coordinate, t – time, $\vec{k}$, ω and $\vec{E}_{\vec{k},\omega}$ are respectively wavenumber, frequency and amplitude of each plane wave $\exp\left(i\vec{k}\vec{r}-i\omega t\right)$. Every such plane wave carries a momentum of $\hbar k$. The dominant momentum in the wavepacket described by (6.1) is inversely proportional to the nanoemitter size *d* as $\langle\hbar k\rangle\sim 2\pi\hbar/d$. For a realistic nanoparticle size of 10nm it is possible to achieve momenta of $\hbar k\sim 0.5\hbar\cdot\mathrm{nm}^{-1}$, which is comparable to typical momenta of charge carriers in solid state systems.

Let us now analyze how an individual high-momentum evanescent wave is absorbed by the most common 2D material – graphene. Graphene's unperturbed Hamiltonian in vicinity of the **K**-point is characterized by a linear dispersion and is written as $H = v_F \vec{p}\vec{\sigma}$. When an evanescent wave carrying a large momentum $\hbar\vec{k}$ is absorbed by graphene, an electron with momentum $\vec{p}$ initially located in the valence band $W_v(\vec{p})$ gets excited into the conduction band W_c with the final momentum $\vec{p}+\hbar\vec{k}$. From the energy conservation law, the energy corresponding to such transition reads

$$W_o^{\vec{k}}(\vec{p}) = W_c\left(\vec{p}+\hbar\vec{k}\right) - W_v(\vec{p}). \tag{6.2}$$

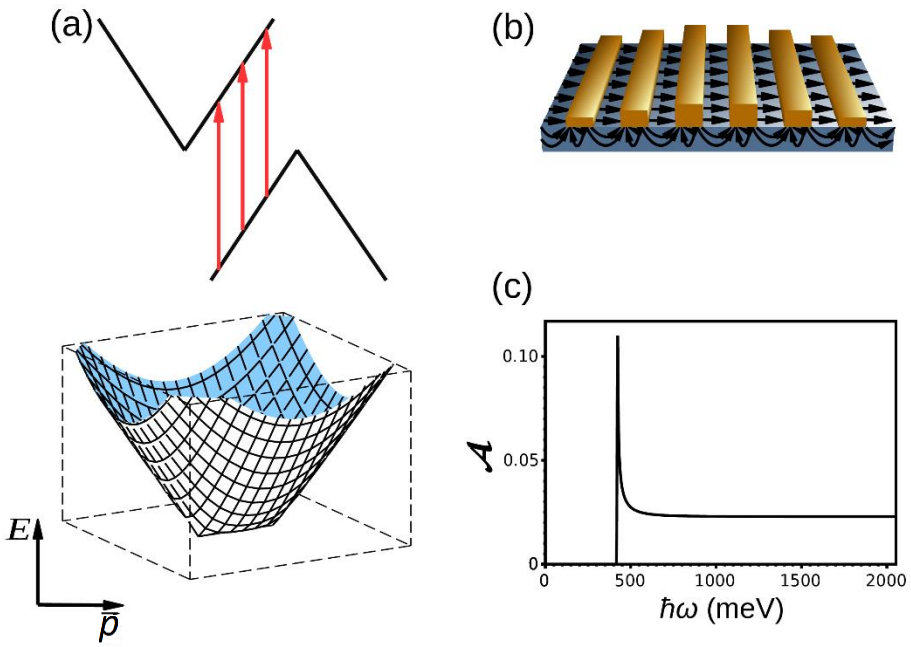

Figure 6.1. Absorption of "high-momentum" evanescent photons. (a) Top: black lines schematically depict graphene bandstructure: energy (vertical axis) as a function of momentum (horizontal axis). Red arrows represent optical transitions. The shift of the conduction and valence bands corresponds to the photon momentum. Bottom: Optical band structure for finite-momentum transitions: transition energy as a function of the wavenumber *p* of a photoexcited electron. **(b)** Design of proposed device consisting of graphene in combination with parallel plasmonic nanostructures. Yellow color depicts metallic nanoparticles; blue color indicates the insulating substrate with a 2D material on top of it and black arrows schematically represent electric field lines. **(c)** Absorption curve (absorbance *vs*. photon energy) calculated for plane waves with a fixed wavelength of 10nm.

We shall call this expression an "optical bandstructure" – transition energy corresponding to the absorption of a photon with an in-plane wavenumber *k* by an electron with initial momentum *p*. It is now instructive to understand the physical significance of the optical bandstructure. Due to the momentum conservation law, electron and hole momenta are not independent. Therefore, given the fixed net momentum *ħk*, the 2-body problem of an electron and a hole can be effectively reduced to a one-body problem characterized by only one momentum value *p*. This reduction is nothing but a well-known procedure of switching to the center-of-mass frame. Thus, in this reduced coordinate system $W_o^{\vec{k}}(\vec{p})$ plays a role of the kinetic energy of an e-h pair in the center-of-mass frame. The typical shape of the graphene optical bandstructure as a function of *p* is shown in Fig. 6.1a.

Based on (6.2) we can evaluate the joint density of states and optical absorption corresponding to such high-momentum transitions. The absorption spectrum of photons with the fixed wavenumber *k* reads:

$$A_{\vec{k}}(\omega) = \pi\alpha \frac{1}{2} \mathrm{Re}\left\{ \left(1 - \left(\frac{v_F k}{\hbar\omega} \right)^2 \right)^{1/2} + \left(1 - \left(\frac{v_F k}{\hbar\omega} \right)^2 \right)^{-1/2} \right\}. \tag{6.3}$$

An example of absorption spectrum of evanescent light waves with k=0.6nm^{-1} is shown in Fig.6.1c. This spectrum is characterized by a strong van Hove singularity that emerges from the second term in (6.3) which has a divergence of the order of $1/\sqrt{\omega - v_F k}$. This singularity, in turn, stems from an effectively one-dimensional groove-like shape of the optical bandstructure for $p << \hbar k$ (Fig.6.1a, bottom). Below the singularity one can also see an emergent optical bandgap. For the future

research, it is interesting to study the effects of Coulomb interactions between photoexcited carriers and investigate a possibility of existence of bound e-h states inside this bandgap.

6.2. Study of novel excitonic species

Continuing the work described in chapter 2, we want to pay more detailed attention to exotic excitonic species. As we have shown in the current work, 2D materials host various excitonic species with unusual dispersion relations: from saddle-point excitons in graphene[21] to MoS_2 excitons with Mexican-hat-shaped dispersion. While kinetic energy of electrons and holes in these excitonic species is well known, it is also interesting to study dispersion of these excitons as a whole: i.e. total exciton energy as a function of the total exciton momentum. Study of dispersion relations of exotic excitons can provide information regarding their dynamical properties, such as effective masses. This is interesting from the point of view of excitonic funneling[157,158] – a novel energy harvesting technique, in which photoexcited excitons are "funneled" to the center of the sample due to induced non-uniform strain of a 2D material. Excitons, efficiently collected in this way can then generate photocurrent or photovoltage. For this technique it is critical to understand the dynamics of these excitons and how they scatter off various impurities. For example, higher effective mass makes it harder to accelerate and transport an exciton, whereas large size increases scattering rate and decreases exciton lifetimes. Studying different materials and excitons with exotic dispersions can lead to discovery of excitons with low effective masses that are very efficient for energy harvesting and excitonic circuitry. For example, as shown in Fig.6.2, bands hosting the C-exciton in TMDCs are locally parallel. According to equation (6.2), on the band diagram level, the kinetic energy of an e-h pair with momentum $\hbar k$ can be represented as a difference between the valence band $W_v(\vec{p})$ and the conduction band

$W_c(\vec{p}+\hbar\vec{k})$ shifted with respect to each other by a wavenumber *k*. Shifting of parallel bands near the **Γ**-point leads to linear, with respect to *k*, shift of the band separation and hence the energy of the electron-hole pair. Thus, it is reasonable to expect the C-exciton to be, in fact, massless – i.e. having linear dependence between energy and momentum of an exciton as a whole.

Moreover, as shown in chapter 2, the C-exciton is strongly de-localized in the momentum space and hence is expected to be highly localized in the real space. Thus, small expected size of the C-exciton may make it less prone to scattering on impurities. Additionally, as we have demonstrated in chapter 2, C-exciton does not require external force to dissociate, which is also beneficial for energy harvesting.

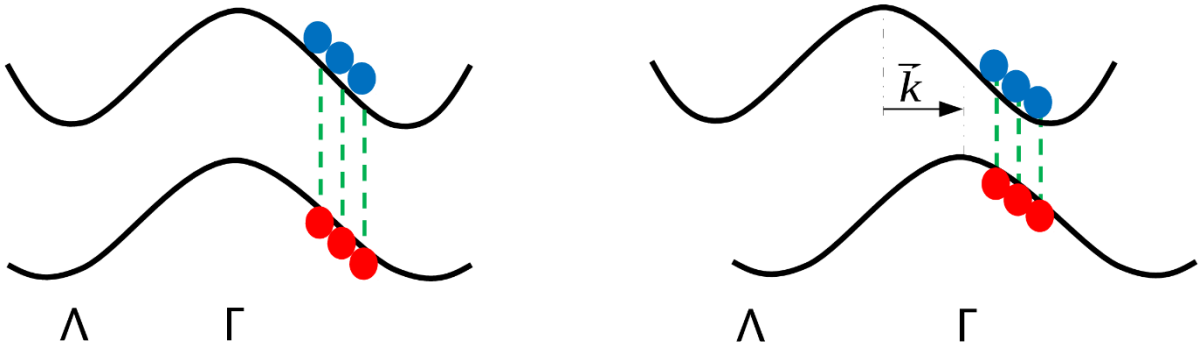

Figure 6.2. Energy of an electron-hole pair at the band nesting area of the Brillouin zone. Left: Band nesting region hosting the C-exciton. Blue and red circles represent electrons and holes respectively. Green dashed lines denote optical transitions. Right: exciton with a non-zero total momentum. According to (6.2) the energy of an e-h pair is evaluated as a difference between valence and conduction bands that are effectively shifted with respect to each other by the wavenumber *k*. This leads to the corresponding decrease of the energy of e-h pairs.

6.3. Further study of dynamic screening

Effects of dynamic screening of excitons in TMDCs, described in chapter 4 can be more thoroughly studied in other nanoscale systems with more controllable interparticle interactions and with easily-obtainable wavefunctions. Precise knowledge of these factors allows to make more

clear and exact predictions of effects of dynamic screening. We propose studying of the following systems:

(1) Weakly-interacting electron-hole pairs in 2D quantum dots. Corresponding wavefunctions and energy levels can be analytically obtained with good precision by solving the "particle in the box" problem. Such states are expected to be symmetric and therefore screened at optical frequencies by the immediate environment of the quantum dot.

(2) Interband Landau level transitions in semiconductors[159]. In the presence of strong magnetic fields of 1 – 10T it is possible to photoexcite electrons and holes existing in quantum Hall states. In this case, wavefunctions and energy levels are also well defined. In the presence of a dynamically screening medium, the self-energy corrections for such pairs can be calculated exactly. Lowest relevant screening frequencies will range from inverse lifetime for asymmetric electron and hole masses to mid-IR region for symmetric ones.

(3) Excited states of excitons. Model described in chapter 4 can be applied not only to the exciton ground state but to excited states as well. For symmetric excitons at higher excited states n, the energy of the first asymmetric transition $E_{n+1,n}$ will decrease with increasing n due to increasing density of excitonic energy levels. Hence, higher excited states will be screened at smaller frequencies than lower ones. These different shifts for different excited states are similar to Lamb shifts in Hydrogen atom or positronium.

BIBLIOGRAPHY

[1] Y. Lin, X. Ling, L. Yu, S. Huang, A. L. Hsu, Y.-H. Lee, J. Kong, M. S. Dresselhaus, and T. Palacios, Nano Letters **14**, 5569 (2014).

[2] A. Chernikov, T. C. Berkelbach, H. M. Hill, A. Rigosi, Y. Li, O. B. Aslan, D. R. Reichman, M. S. Hybertsen, and T. F. Heinz, Physical Review Letters **113**, 076802 (2014).

[3] A. G. Walsh, A. N. Vamivakas, Y. Yin, S. B. Cronin, M. S. Ünlü, B. B. Goldberg, and A. K. Swan, Nano letters **7**, 1485 (2007).

[4] K. Andersen, S. Latini, and K. S. Thygesen, Nano letters **15**, 4616 (2015).

[5] K. F. Mak, C. Lee, J. Hone, J. Shan, and T. F. Heinz, Physical Review Letters **105**, 136805 (2010).

[6] K. S. Novoselov, A. K. Geim, S. Morozov, D. Jiang, M. Katsnelson, I. Grigorieva, S. Dubonos, and A. Firsov, nature **438**, 197 (2005).

[7] H. R. Gutiérrez *et al.*, Nano letters **13**, 3447 (2012).

[8] G. Plechinger, P. Nagler, J. Kraus, N. Paradiso, C. Strunk, C. Schüller, and T. Korn, physica status solidi (RRL)-Rapid Research Letters **9**, 457 (2015).

[9] A. Chernikov, A. M. van der Zande, H. M. Hill, A. F. Rigosi, A. Velauthapillai, J. Hone, and T. F. Heinz, Physical review letters **115**, 126802 (2015).

[10] B. Zhu, X. Chen, and X. Cui, Scientific Reports **5**, 9218 (2015).

[11] A. Ramasubramaniam, Physical Review B **86**, 115409 (2012).

[12] M. Dendzik *et al.*, Physical Review B **92**, 245442 (2015).

[13] K. F. Mak, C. Lee, J. Hone, J. Shan, and T. F. Heinz, Physical Review Letters **105**, 136805 (2010).

[14] P. Rivera *et al.*, Nature communications **6**, 6242 (2015).

[15] L. V. Keldysh, Pisma Zh. Eksp. Teor. Fiz **29**, 658 (1979).

[16] T. C. Berkelbach, M. S. Hybertsen, and D. R. Reichman, Physical Review B **88**, 045318 (2013).

[17] K. I. Bolotin, K. Sikes, Z. Jiang, M. Klima, G. Fudenberg, J. Hone, P. Kim, and H. Stormer, Solid State Communications **146**, 351 (2008).

[18] Y. Zhang, Y.-W. Tan, H. L. Stormer, and P. Kim, Nature **438**, 201 (2005).

[19] K. I. Bolotin, F. Ghahari, M. D. Shulman, H. L. Stormer, and P. Kim, Nature **462**, 196 (2009).

[20] R. R. Nair, P. Blake, A. N. Grigorenko, K. S. Novoselov, T. J. Booth, T. Stauber, N. M. Peres, and A. K. Geim, Science **320**, 1308 (2008).

[21] P. Yadav, P. K. Srivastava, and S. Ghosh, Nanoscale **7**, 18015 (2015).

[22] B. W. Baugher, H. O. Churchill, Y. Yang, and P. Jarillo-Herrero, Nano letters **13**, 4212 (2013).

[23] K. Watanabe, T. Taniguchi, and H. Kanda, Nature materials **3**, 404 (2004).

[24] C. Steinborn, M. Herrmann, U. Keitel, A. Schönecker, J. Räthel, D. Rafaja, and J. Eichler, Journal of the European Ceramic Society **33**, 1225 (2013).

[25] W. Krätschmer, L. D. Lamb, K. Fostiropoulos, and D. R. Huffman, Nature **347**, 27 (1990).

[26] A. P. Alivisatos, Science **271**, 933 (1996).

[27] S. Mouri, Y. Miyauchi, and K. Matsuda, Nano letters **13**, 5944 (2013).

[28] A. Das *et al.*, Nature nanotechnology **3**, 210 (2008).

[29] B. Sachs, L. Britnell, T. O. Wehling, A. Eckmann, R. Jalil, B. D. Belle, A. I. Lichtenstein, M. I. Katsnelson, and K. S. Novoselov, Applied Physics Letters **103**, 251607 (2013).

[30] S. Ghatak, A. N. Pal, and A. Ghosh, Acs Nano **5**, 7707 (2011).

[31] A. Newaz, D. Prasai, J. Ziegler, D. Caudel, S. Robinson, R. Haglund Jr, and K. Bolotin, Solid State Communications **155**, 49 (2013).

[32] C. B. Murphy, Y. Zhang, T. Troxler, V. Ferry, J. J. Martin, and W. E. Jones, The Journal of Physical Chemistry B **108**, 1537 (2004).

[33] D. Prasai *et al.*, Nano Letters **15**, 4374 (2015).

[34] A. Raja *et al.*, Nano letters **16**, 2328 (2016).

[35] A. Newaz, Y. S. Puzyrev, B. Wang, S. T. Pantelides, and K. I. Bolotin, Nature communications, **3**, 734 (2012).

[36] Q. H. Wang, K. Kalantar-Zadeh, A. Kis, J. N. Coleman, and M. S. Strano, Nat Nano **7**, 699 (2012).

[37] D. Y. Qiu, F. H. da Jornada, and S. G. Louie, Phys Rev Lett **111**, 216805 (2013).

[38] K. F. Mak, C. Lee, J. Hone, J. Shan, and T. F. Heinz, Phys Rev Lett **105**, 136805 (2010).

[39] K. I. Bolotin, K. J. Sikes, Z. Jiang, M. Klima, G. Fudenberg, J. Hone, P. Kim, and H. L. Stormer, Solid State Communications **146**, 351 (2008).

[40] T. Jin, J. Kang, E. Su Kim, S. Lee, and C. Lee, Journal of Applied Physics **114**, 164509 (2013).

[41] L. Britnell *et al.*, Science **340**, 1311 (2013).

[42] O. Lopez-Sanchez, D. Lembke, M. Kayci, A. Radenovic, and A. Kis, Nat Nanotechnol **8**, 497 (2013).

[43] M. Bernardi, M. Palummo, and J. C. Grossman, Nano Lett **13**, 3664 (2013).

[44] B. W. H. Baugher, H. O. H. Churchill, Y. Yang, and P. Jarillo-Herrero, Nano Lett **13**, 4212 (2013).

[45] W. Z. Bao, X. H. Cai, D. Kim, K. Sridhara, and M. S. Fuhrer, Appl Phys Lett **102**, 4 (2013).

[46] B. Radisavljevic and A. Kis, Nat Mater **12**, 815 (2013).

[47] G. Eda, H. Yamaguchi, D. Voiry, T. Fujita, M. W. Chen, and M. Chhowalla, Nano Lett **12**, 526 (2012).

[48] C. Soci, A. Zhang, X. Y. Bao, H. Kim, Y. Lo, and D. L. Wang, J Nanosci Nanotechno **10**, 1430 (2010).

[49] R. T. Collins, K. v. Klitzing, and K. Ploog, Physical Review B **33**, 4378 (1986).

[50] J. D. Mar, J. J. Baumberg, X. L. Xu, A. C. Irvine, C. R. Stanley, and D. A. Williams, Physical Review B **87**, 155315 (2013).

[51] M. Buscema, M. Barkelid, V. Zwiller, H. S. J. van der Zant, G. A. Steele, and A. Castellanos-Gomez, Nano Lett **13**, 358 (2013).

[52] D. S. Chemla and J. Shah, Nature **411**, 549 (2001).

[53] K. K. Kam and B. A. Parkinson, J Phys Chem-Us **86**, 463 (1982).

[54] P. Nagpal and V. I. Klimov, Nat communications **2**, 486 (2011).

[55] M. Freitag, T. Low, F. N. Xia, and P. Avouris, Nat Photonics **7**, 53 (2013).

[56] G. Konstantatos, M. Badioli, L. Gaudreau, J. Osmond, M. Bernechea, F. P. G. de Arquer, F. Gatti, and F. H. L. Koppens, Nat Nanotechnol **7**, 363 (2012).

[57] A. Splendiani, L. Sun, Y. B. Zhang, T. S. Li, J. Kim, C. Y. Chim, G. Galli, and F. Wang, Nano Lett **10**, 1271 (2010).

[58] D. Xiao, G. B. Liu, W. X. Feng, X. D. Xu, and W. Yao, Phys Rev Lett **108**, 19 (2012).

[59] A. Molina-Sánchez, D. Sangalli, K. Hummer, A. Marini, and L. Wirtz, Phys. Rev. B **88**, 045412 (2013).

[60] M. Rohlfing and S. G. Louie, Physical Review B **62**, 4927 (2000).

[61] F. Hüser, T. Olsen, and K. S. Thygesen, Physical Review B **88**, 245309 (2013).

[62] B. Skinner, B. I. Shklovskii, and M. B. Voloshin, Physical Review B **89**, 041405 (2014).

[63] K. Dolui, I. Rungger, and S. Sanvito, Physical Review B **87**, 165402 (2013).

[64] S. Tongay *et al.*, Sci. Rep. **3**, 2657 (2013).

[65] K. F. Mak, K. L. He, C. Lee, G. H. Lee, J. Hone, T. F. Heinz, and J. Shan, Nat Mater **12**, 207 (2013).

[66] J. S. Ross *et al.*, Nat Commun **4**, 1474 (2013).

[67] X. L. Yang, S. H. Guo, F. T. Chan, K. W. Wong, and W. Y. Ching, Physical Review A **43**, 1186 (1991).

[68] H.-P. Komsa and A. V. Krasheninnikov, Physical Review B **86**, 241201 (2012).

[69] L. A. Ribeiro, P. H. Oliveira Neto, W. F. da Cunha, L. F. Roncaratti, R. Gargano, D. A. da Silva Filho, and G. M. e Silva, The Journal of Chemical Physics **135**, 224901 (2011).

[70] A. D. Mohite, P. Gopinath, H. M. Shah, and B. W. Alphenaar, Nano Lett **8**, 142 (2008).

[71] B. A. Gregg, J Phys Chem B **107**, 4688 (2003).

[72] C.-C. Wu, D. Jariwala, V. K. Sangwan, T. J. Marks, M. C. Hersam, and L. J. Lauhon, The Journal of Physical Chemistry Letters **4**, 2508 (2013).

[73] Z. Yin *et al.*, ACS Nano **6**, 74 (2011).

[74] D.-S. Tsai, K.-K. Liu, D.-H. Lien, M.-L. Tsai, C.-F. Kang, C.-A. Lin, L.-J. Li, and J.-H. He, ACS Nano **7**, 3905 (2013).

[75] K. K. Ng, *Complete guide to semiconductor devices* (J. Wiley & Sons, New York, 2002), 2nd edn., pp. P 439-444.

[76] M. Fontana, T. Deppe, A. K. Boyd, M. Rinzan, A. Y. Liu, M. Paranjape, and P. Barbara, Sci. Rep. **3** (2013).

[77] H. C. Liu, J. Li, J. R. Thompson, Z. R. Wasilewski, M. Buchanan, and J. G. Simmons, Electron Device Letters, IEEE **14**, 566 (1993).

[78] G. Eda and S. A. Maier, ACS Nano **7**, 5660 (2013).

[79] B. Zhu, X. Chen, and X. Cui, arXiv:1403.5108 (2014).

[80] Z. Ye, T. Cao, K. O'Brien, H. Zhu, X. Yin, Y. Wang, S. G. Louie, and X. Zhang, arXiv:1403.5568 (2014).

[81] G. Wang, X. Marie, I. Gerber, T. Amand, D. Lagarde, L. Bouet, M. Vidal, A. Balocchi, and B. Urbaszek, arXiv:1404.0056 (2014).

[82] A. Chernikov, T. C. Berkelbach, H. M. Hill, A. Rigosi, Yilei Li, Özgur B. Aslan, David R. Reichman, a. Mark S. Hybertsen, and T. F. Heinz, arXiv:1403.4270 (2014).

[83] K. He, N. Kumar, L. Zhao, Z. Wang, K. F. Mak, H. Zhao, and J. Shan, Phys Rev Lett **113**, 026803 (2014).

[84] R. S. Swathi and K. L. Sebastian, J. Chem. Phys. **130**, 086101 (2009).

[85] A. K. M. Newaz, D. Prasai, J. I. Ziegler, D. Caudel, S. Robinson, R. F. Haglund Jr, and K. I. Bolotin, Sol. Stat. Comm. **155**, 49 (2013).

[86] K. F. Mak, K. He, C. Lee, G. H. Lee, J. Hone, T. F. Heinz, and J. Shan, Nat. Mater. **12**, 207 (2013).

[87] J. S. Ross *et al.*, Nat. Commun. **4**, 1474 (2013).

[88] F. Wang, Y. Zhang, C. Tian, C. Girit, A. Zettl, M. Crommie, and Y. R. Shen, Science **320**, 206 (2008).

[89] K. Mak, C. Lee, J. Hone, J. Shan, and T. Heinz, Phys. Rev. Lett. **105**, 136805 (2010).

[90] A. Splendiani, L. Sun, Y. Zhang, T. Li, J. Kim, C.-Y. Chim, G. Galli, and F. Wang, Nano. Lett. **10**, 1271 (2010).

[91] A. R. Klots *et al.*, Sci. Rep. **4**, 6608 (2014).

[92] A. Chernikov, T. C. Berkelbach, H. M. Hill, A. Rigosi, Y. Li, O. B. Aslan, D. R. Reichman, M. S. Hybertsen, and T. F. Heinz, Physical Review Letters **113**, 076802 (2014).

[93] Z. Ye, T. Cao, K. O/'Brien, H. Zhu, X. Yin, Y. Wang, S. G. Louie, and X. Zhang, Nature **513**, 214 (2014).

[94] J. Lee, W. Bao, L. Ju, P. J. Schuck, F. Wang, and A. Weber-Bargioni, Nano. Lett. **14**, 7115 (2014).

[95] K. J. Tielrooij *et al.*, Nat. Phys. **11**, 281 (2015).

[96] F. Xia, H. Wang, D. Xiao, M. Dubey, and A. Ramasubramaniam, Nat. Photon. **8**, 899 (2014).

[97] R. M. Clegg, in *Laboratory Techniques in Biochemistry and Molecular Biology*, edited by T. W. J. Gadella (Elsevier, 2009), p. 1

[98] F. Federspiel *et al.*, Nano. Lett. **15** (2), 1252-1258 (2015).

[99] C. Zhang, H. Wang, W. Chan, C. Manolatou, and F. Rana, Phys. Rev. B **89**, 205436 (2014).

[100] S. Schmitt-Rink, D. S. Chemla, and D. A. B. Miller, Adv. Phys. **38**, 89 (1989).

[101] M. A. Harrison, A. Ng, A. B. Hmelo, and S. J. Rosenthal, Isr. J. Chem. **52**, 1063 (2012).

[102] I. Hemdana, M. Mahdouani, and R. Bourguiga, Phys. B: Cond. Matt. **407**, 3313 (2012).

[103] T. Korn, S. Heydrich, M. Hirmer, J. Schmutzler, and C. Schüller, Appl. Phys. Lett. **99**, 102109 (2011).

[104] M.-Q. Zhu, E. Chang, J. Sun, and R. A. Drezek, J. Mat. Chem. **17**, 800 (2007).

[105] S. Ravindran, S. Chaudhary, B. Colburn, M. Ozkan, and C. S. Ozkan, Nano. Lett. **3**, 447 (2003).

[106] A. A. Gunawan, B. Chernomordik, D. Plemmons, D. Deng, E. Aydil, and A. Mkhoyan, Microsc. Microanal. **19**, 1506 (2013).

[107] C. R. Dean *et al.*, Nat. Nano. **5**, 722 (2010).

[108] P. J. Zomer, S. P. Dash, N. Tombros, and B. J. van Wees, Appl. Phys. Lett. **99**, 232104 (2011).

[109] Z. Chen, S. Berciaud, C. Nuckolls, T. F. Heinz, and L. E. Brus, ACS Nano **4**, 2964 (2010).

[110] F. Prins, A. J. Goodman, and W. A. Tisdale, Nano. Lett. **14**, 6087 (2014).

[111] S. N. Sharma, Z. S. Pillai, and P. V. Kamat, J. Phys. Chem. B **107**, 10088 (2003).

[112] P. P. Jha and P. Guyot-Sionnest, J. Phys. Chem. C **111**, 15440 (2007).

[113] P. P. Jha and P. Guyot-Sionnest, J. Phys. Chem. C **114**, 21138 (2010).

[114] S. Li, M. L. Steigerwald, and L. E. Brus, ACS Nano **3**, 1267 (2009).

[115] R. Geick, C. H. Perry, and G. Rupprecht, Physical Review **146**, 543 (1966).

[116] X. Chen *et al.*, Nat. Commun. **6**, 6088 (2015).

[117] D. Efetov, P. Maher, S. Glinskis, and P. Kim, Phys. Rev. B **84**, 161412 (2011).

[118] S. Empedocles, D. Norris, and M. Bawendi, Phys. Rev. Lett. **77**, 3873 (1996).

[119] W. Zhao, Z. Ghorannevis, L. Chu, M. Toh, C. Kloc, P.-H. Tan, and G. Eda, ACS Nano **7**, 791 (2013).

[120] S. Liu, N. J. Borys, J. Huang, D. V. Talapin, and J. M. Lupton, Phys. Rev. B **86**, 045303 (2012).

[121] A. J. Bennett, R. B. Patel, J. Skiba-Szymanska, C. A. Nicoll, I. Farrer, D. A. Ritchie, and A. J. Shields, Appl. Phys. Lett. **97**, 031104 (2010).

[122] A. M. van der Zande *et al.*, Nat. Mater. **12**, 554 (2013).

[123] Y.-H. Lee *et al.*, Adv. Mater. **24**, 2320 (2012).

[124] N. J. Orfield, J. R. McBride, J. D. Keene, L. M. Davis, and S. J. Rosenthal, ACS Nano **9**, 831 (2015).

[125] J. Eisenstein and A. MacDonald, Nature **432**, 691 (2004).

[126] A. M. Jones *et al.*, Nature nanotechnology **8**, 634 (2013).

[127] A. Mysyrowicz, D. Hulin, A. Antonetti, A. Migus, W. Masselink, and H. Morkoc, Physical review letters **56**, 2748 (1986).

[128] N. Peyghambarian, S. Park, S. W. Koch, A. Jeffery, J. Potts, and H. Cheng, Applied physics letters **52**, 182 (1988).

[129] A. Raja *et al.*, arXiv preprint arXiv:1702.01204 (2017).

[130] R. Zimmermann, K. Kilimann, W. Kraeft, D. Kremp, and G. Röpke, physica status solidi (b) **90**, 175 (1978).

[131] H. Haug and S. Schmitt-Rink, Progress in Quantum Electronics **9**, 3 (1984).

[132] J. Gay, Physical Review B **4**, 2567 (1971).

[133] D. Ninno, F. Liguori, V. Cataudella, and G. Iadonisi, Journal of Physics: Condensed Matter **6**, 9335 (1994).

[134] S. Ikeda, M. Yamashita, and C. Otani, in *2014 39th International Conference on Infrared, Millimeter, and Terahertz waves (IRMMW-THz)* (IEEE, 2014), pp. 1.

[135] C. Wakai, A. Oleinikova, M. Ott, and H. Weingärtner, The Journal of Physical Chemistry B **109**, 17028 (2005).

[136] S. Seki, S. Tsuzuki, K. Hayamizu, Y. Umebayashi, N. Serizawa, K. Takei, and H. Miyashiro, Journal of Chemical & Engineering Data **57**, 2211 (2012).

[137] X. Yan, L. Zhu, Y. Zhou, E. Yiwen, L. Wang, and X. Xu, Applied optics **54**, 6732 (2015).

[138] H. Bethe, L. Brown, and J. Stehn, Physical Review **77**, 370 (1950).

[139] M. E. Peskin, Schroeder, V. S., *Introduction to Quantum Field Theory* (Perseus Book Publishing, 1995), 2 edn., pp. 228-250.

[140] S. Tongay *et al.*, Scientific reports **3**, 2657 (2013).

[141] P. K. Chow, R. B. Jacobs-Gedrim, J. Gao, T.-M. Lu, B. Yu, H. Terrones, and N. Koratkar, ACS nano **9**, 1520 (2015).

[142] C. Lui, A. Frenzel, D. Pilon, Y.-H. Lee, X. Ling, G. Akselrod, J. Kong, and N. Gedik, Physical review letters **113**, 166801 (2014).

[143] R. Schmidt, G. Berghäuser, R. Schneider, M. Selig, P. Tonndorf, E. Malic, A. Knorr, S. Michaelis de Vasconcellos, and R. Bratschitsch, Nano letters **16**, 2945 (2016).

[144] H. Yu, G. Liu, P. Gong, X. Xu, and W. Yao, arXiv preprint arXiv:1401.0667 (2014).

[145] P. Zomer, S. Dash, N. Tombros, and B. Van Wees, Applied Physics Letters **99**, 232104 (2011).

[146] H. J. Conley, B. Wang, J. I. Ziegler, R. F. Haglund Jr, S. T. Pantelides, and K. I. Bolotin, Nano letters **13**, 3626 (2013).

[147] H. Nan *et al.*, ACS nano **8**, 5738 (2014).

[148] A. R. Klots *et al.*, Scientific Reports **4**, 6608 (2014).

[149] A. Molina-Sánchez, D. Sangalli, K. Hummer, A. Marini, and L. Wirtz, Physical Review B **88**, 045412 (2013).

[150] D. W. Kidd, D. K. Zhang, and K. Varga, Physical Review B **93**, 125423 (2016).

[151] J. Mitroy *et al.*, Reviews of Modern Physics **85**, 693 (2013).

[152] K. Varga, Computer Physics Communications **179**, 591 (2008).

[153] K. A. Velizhanin and A. Saxena, Physical Review B **92**, 195305 (2015).

[154] D. Y. Qiu, H. Felipe, and S. G. Louie, Physical review letters **111**, 216805 (2013).

[155] C. Zhang, A. Johnson, C.-L. Hsu, L.-J. Li, and C.-K. Shih, Nano letters **14**, 2443 (2014).

[156] M. J. Bowers, J. R. McBride, and S. J. Rosenthal, Journal of the American Chemical Society **127**, 15378 (2005).

[157] T. A. Klar, T. Franzl, A. L. Rogach, and J. Feldmann, Advanced Materials **17**, 769 (2005).

[158] P. San-Jose, V. Parente, F. Guinea, R. Roldán, and E. Prada, Physical Review X **6**, 031046 (2016).

[159] V. Gusynin, S. Sharapov, and J. Carbotte, Journal of Physics: Condensed Matter **19**, 026222 (2006).